Leidenfrost Effect and Coarsening in a Granular Gas

Peter Eshuis

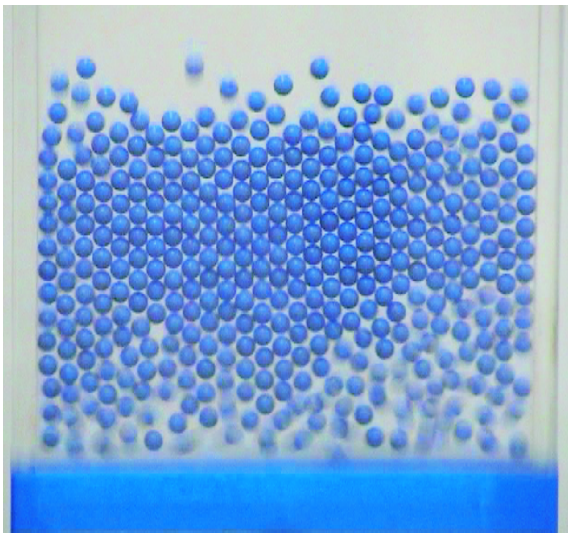

Master Thesis
P.G. Eshuis, studentnr: 9801286

August 29th, 2003

University of Twente
Department of Applied Physics
Physics of Fluids Group

Graduation Committee:
Prof. Dr. D. Lohse
Dr. K. van der Weele
Drs. D. van der Meer
Ir. A. den Ouden

Printed in The Netherlands.

Typeset by the author using LaTeX.

The cover picture on the left shows a typical experimental image of the Granular Leidenfrost Effect and the picture on the right shows the initial condition of a Granular Coarsening experiment.

"Παντα ρει" or "Panta rei"

"Everything flows", already known by the Greek philosopher Herakleitos (535-475 BC).

Samenvatting

Granulair materiaal (of granulaten) kun je overal om je heen vinden: een paar voorbeelden zijn zand, suiker of in het algemeen "korrelvormige materialen". Het lijken zulke gewone materialen, maar ze kennen zeer verschillende verschijningsvormen. Granulaten kunnen zich namelijk gedragen als een vaste stof, denk maar aan een doodnormaal hoopje zand. Verder gedragen ze zich als een (bijzondere) vloeistof in een zandloper en in de door mij uitgevoerde experimenten gedragen de glazen kogeltjes zich als een gas, doordat we hard schudden.
Het onderzoek naar granulaten is van fundamenteel belang, want vele eigenschappen van granulaire systemen zijn nog niet geheel verklaard. Daarnaast gebruiken allerlei industrieën granulaten als basis- of eindprodukt. Voor deze zeer uiteenlopende industrieën is het zeer van belang om deze speciale soort stoffen goed te doorgronden. Bij de farmaceutische industrie bijvoorbeeld is het zeer ongewenst als bij de productie van pillen alle werkzame stof in één pilletje komt te zitten, doordat de verschillende poeders gaan scheiden (een veelvoorkomend granulair verschijnsel). Geschat wordt dat ongeveer 40% van de industriële capaciteit en energie wordt verspild door problemen met granulaire materialen!

Mijn afstudeerwerk beslaat twee onderwerpen:

- Het Leidenfrost effect in een granulair gas
- "Coarsening" (verruwing) in een granulair gas

Het Leidenfrost effect in een granulair gas
Het "Leidenfrost effect" is het intrigerende fenomeen dat een druppel water op een gloeiend hete plaat niet direct verdampt, maar juist zeer lang op deze gloeiende plaat kan blijven liggen. Dit effect kan zelfs langer dan een minuut duren!
De verklaring voor dit verrassende effect ligt in het feit dat wanneer de temperatuur van de plaat boven de 200 graden Celsius ligt, de druppel direct een laagje waterdamp vormt. Dit zeer dunne laagje zorgt ervoor dat er alleen een slechte, indirecte warmte-overdracht van de plaat naar de druppel plaats kan vinden. Zo kan onze druppel als een ware hovercraft meer dan een minuut over de hete plaat dansen.
De granulaire versie van dit effect kun je waarnemen, wanneer je een plat bakje (diepte net iets meer dan de diameter van een kogeltje) vult met glazen kogeltjes. Bij voldoende hard schudden zal er namelijk een cluster van dicht opeengepakte (en daardoor langzame) kogeltjes gaan zweven. Onder en boven dit cluster bevinden zich minder dicht opeengepakte

kogeltjes, die heel snel bewegen. Dit betekent dat een "koud" cluster, waarin de kogeltjes relatief langzaam bewegen, boven en onder wordt omgeven door "hete", snelle kogeltjes. Bij het oorspronkelijke Leidenfrost effect hadden we ook een koud cluster, de druppel, die omgeven was door een hete omgeving. Vandaar dat dit experiment de granularie versie van het Leidenfrost effect wordt genoemd.
Uit de Granulaire Leidenfrost experimenten heb ik diverse eigenschappen van dit specifieke systeem gehaald: wanneer je de schudsterkte langzaam opvoert is er een moment dat het cluster gaat zweven. Deze fase-overgang heb ik geanalyseerd, waarbij ik het aantal lagen kogeltjes en de schudsterkte onafhankelijk van elkaar heb gevarieerd. Hieruit blijkt de genoemde fase-overgang naar een zwevend cluster steeds voor dezelfde waarde van de schudsterkte $S \approx (af)^2$ te gebeuren (a is de amplitude van het schudden en f de frequentie).

"Coarsening" (verruwing) in een granulair gas
Het effect van "coarsening", ook wel verruwing, kun je heel goed zien wanneer je een vers getapt biertje met een goede schuimkraag bekijkt. Het gaat dan vooral eventjes om deze schuimkraag: wanneer je hier een hele tijd naar blijft kijken, dan kun je de vele kleine celletjes van het schuim zien samensmelten met wat grotere cellen. Dit proces van grote cellen die kleintjes opeten heet "coarsening" en gaat onverminderd door totdat enkel nog grote cellen overblijven, die uiteindelijk knappen. Voila... een doodgeslagen biertje!
In de door mij gebruikte ringvormige opstelling met 12 bakjes is hetzelfde proces te zien wanneer je in elk bakje evenveel kogeltjes doet. Bij een bepaalde schudsterkte zullen de kogeltjes van bakje naar bakje springen en door toevallige fluctuaties zullen er soms onevenredig veel kogeltjes in één bakje terecht komen, oftewel er vormt zich een cluster van kogeltjes in dit bakje. Van de 12 bakjes kunnen er dan bijvoorbeeld op een gegeven moment 3 een cluster bevatten en omdat in deze clusters veel botsingen plaatsvinden, is de kans klein dat een kogeltje weer uit het bakje springt. Kortom, de goed gevulde clusters (veel kogeltjes in een bakje) verzamelen daardoor steeds meer kogeltjes uit de bakjes met weinig kogeltjes. Net als bij de schuimkraag eten de grote clusters de kleine op, dus vandaar dat deze experimenten de granulaire "coarsening" experimenten heten. En ook hier gaat dit proces door, zodat eerst 3 clusters onstaan. Ook deze 3 clusters eten elkaar op, al duurt het wat langer, maar uiteindelijk zal er slechts 1 cluster overblijven. Dit is de enige stabiele eindsituatie voor dit systeem.
Uit het hierboven beschreven experiment heb ik enkele voorspellingen van de bestaande theorie proberen te controleren, zoals de tijd die het duurt voordat het winnende cluster is gevormd enz. De resultaten van deze experimenten komen over het algemeen goed overeen met de theorie.

Abstract

Leidenfrost effect:

In a vertically vibrated quasi-2D container filled with glass beads (d = 4.0 mm) a density inverted state is reached through a second order phase transition. Above a critical shaking strength, and for a sufficient number of layers ($F \geq 10$), a cluster of beads is elevated and supported by a few fast particles underneath the cluster. This cluster exhibits an almost perfect hexagonal close packing, causing the density to be maximal at the floating cluster and distinctly lower above and below this cluster. This means that the particles are moving faster and the granular temperature below and above the cluster is, and remains, higher than in the cluster itself: the Granular Leidenfrost effect.
The adapted continuum model based on the hydrodynamic equations is found to be in qualitative agreement as far as the density profiles for various shaking strength are concerned. However, these profiles do not exhibit the experimentally observed feature of getting a density inverted state above a critical shaking strength only. The results from the theoretical model show density inversion for all shaking strengths for more than $F > 3$ layers and no inversion for $F \leq 3$. Thus, no second order phase transition is recovered in the current theoretical model.
The experimental results at the transition to density inversion together with the formulated continuum theory gives confidence that shaking strength $S = \Gamma A \propto (af)^2$ is the important control parameter, which is constant at this second order phase transition.

Coarsening:

Two types of granular experiments have been performed with a ring setup consisting of $N = 12$ compartments:

Uniform Distribution: Starting from a uniform distribution using $P = 480$ glass beads in total, the ring setup is shaken at various shaking strengths. Analysis of the experimental pictures showed that no quantitative information can be extracted concerning the particle fraction n_k profile of the compartments between two clusters.
In agreement with the existing theory in the experiments at low shaking strength more (unstable) transient states are observed (and also for a longer time) than for a higher shaking strength.

Two Clusters: The other experiments started with two competing clusters ($P = 200$ and $P = 280$ beads) a certain number of compartments d apart in the ring setup. The interaction between the two clusters can act through two paths: the shorter path d, but also along the longer path with distance $12 - d$ ($d \leq 6$). The time it takes before one of the clusters breaks down is predicted by the flux model:

$$t_{breakdown} = t_0 d(1 - \frac{d}{12}), \tag{1}$$

where t_0 is the breakdown time for two clusters situated next to each other. The experimental results show that this prediction for the breakdown time holds for small inter-cluster distances: $d \leq 3$. However, the experiments with two clusters a distance $d > 3$ apart are not in agreement with this relation. The corresponding breakdown times show a saturation, indicating a lack of interaction between the two clusters. The proposed explanation is that the smaller cluster ($P = 200$) breaks down via a phenomenon called "sudden collapse", before any significant interaction between the clusters has taken place. Thus, for $d > 3$ the two clusters are acting as two independent clusters. This saturation effect has also been reported in Molecular Dynamics simulations.

Acknowledgements

This report of my master work brings an end to the time of being a student, but I am glad my time in the Physics of Fluids group is not over yet. The collaboration with Ko van der Weele (my supervisor), Detlef Lohse (chairholder) and Devaraj van der Meer was very motivating and constructive. A special word of thanks I want to direct to my supervisor, Ko van der Weele, because we spent many hours together discussing the theory, experiments and the results. He inspired me every time with critical remarks and useful suggestions, and he always had time for some small talk too!

The reflections during the regular granular group-meetings with Detlef Lohse, Ko van der Weele, Devaraj van der Meer, René Mikkelsen and Raymond Bergmann were very useful for the progress of my master work. Hereby I would like to thank these granular people to cluster with me in Detlef's room!

I would like to take this opportunity also to thank Gert-Wim Bruggert, our technician. He made some really beautiful setups and always had time to help me out if there occurred to be a problem. Our administrator, Bas Benschop, and former master student Roy Ikink, helped me out whenever I had a "problem" with my computer, which I appreciated very much. I am also grateful to the D2-project group consisting of Timo Rozendal, Daan Martens and Carel Crane for doing a great job on the granular coarsening experiments in such a short period of time. Last but not least, I want to thank all the master students I have interacted with and made the last year a very pleasant time.

As mentioned above, I am going to perform more research during my PhD-project for the next four years. I am very grateful Detlef Lohse offered me this opportunity and I am looking forward to the continued collaboration with the Physics of Fluids Group!

Peter Eshuis
August 29th, 2003

Contents

Chapter 1

Introduction

1.1 What is Granular Matter?

Granular matter is everywhere in everyday life: a few examples are sand, salt, sugar, gravel or any grain like material in general. These materials seem so simple, but they contain many not fully understood features. Granular matter can behave like all three states of matter, for example in a sandpile at rest, the granular material acts like a solid, see the dune in Fig. 1.1. In an hourglass the sand particles are flowing, therefore the sand is clearly behaving as a liquid in an hourglass. The third state of matter, gas, is present in the granular experiments discussed in this thesis: Granular matter can act as a granular gas when shaken above a certain critical shaking strength. See the review articles by Jaeger, Nagel and Behringer [1, 2], Goldhirsch [3] and Kadanoff [4].

Figure 1.1: a) An example of a granular solid is this dune (or large sandpile) at rest. b) Liquid-like behavior of sand can be observed in a hourglass. c) Granular material is behaving as a gas in an experiment discussed in this thesis, when it is shaken above a critical shaking strength.

From a fundamental point of view it is very interesting to investigate granular phenomenon more in detail, because only a few granular effects have been fully explained up till now. Furthermore, many industries are involved in processing, transporting or storing granular materials, so it is a major concern to reveal all the secrets of granular materials to efficiently work with these materials. It is clear for example that the pharmaceutical industry has to be careful while handling powders to produce pills, because every pill has to contain the same amount of effective substance. So size segregation, often observed in granular experiments, is something the pharmaceutical industry wants to prevent. According to an estimate by Knowlton et al. [5], every year over 1000 silos, bins and hoppers fail in North America just like in Fig. 1.2. Considering all problems arising from handling granular materials in industries like the ones mentioned above, it is argued that about 40% of the industrial capacity is wasted due to these problems. Therefore, it is very important to understand how granular materials act in general [1, 2].

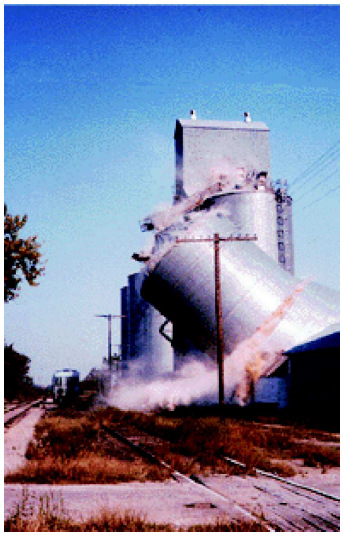

Figure 1.2: Industries handling granular materials often encounter problems of which this collapsing bin is a disastrous example... (from [6])

1.2 Granular Matter acting as a Gas

This master thesis treats two systems in which granular matter, glass beads, acts like a gas due to shaking the setup above a certain shaking strength. The granular particles are non-cohesive and the particle collisions are inelastic. This means that in each collision energy is dissipated. This property of a granular gas is the main reason why it behaves so distinctively different from ordinary gases.
Another difference is the fact that in a granular gas the ordinary energy scale, k_BT, is effectively zero. This is due to the fact that heat is not able to move grains larger than

$\sim$1 micron. So in granular systems the potential energy, mgd, is the relevant energy scale. This means that ordinary thermodynamic arguments do not apply in granular systems and when a granular system is shaken it can be considered to be far from equilibrium. When you consider size segregation in a granular experiment as mentioned in section 1.1, for example, it intuitively contradicts the principle of increasing entropy. However, this thermodynamic principle is completely outclassed by the dynamical effects in granular matter. Because ordinary temperature is not a useful concept in granular systems, the "granular temperature" is defined: $T \propto \langle \boldsymbol{v}^2 \rangle$, i.e. the mean squared velocity of the particles. Whenever the temperature or T is mentioned in this thesis, the granular temperature is considered.

This report is divided into two parts:

- **Part I: Leidenfrost Effect in a Granular Gas**
  This part deals with the experimental results and theory of a quasi-2D experiment, which exhibits a phenomenon called the "Granular Leidenfrost Effect".
- **Part II: Coarsening in a Granular Gas**
  The results of the experiments in a ring setup consisting of 12 compartments will be compared with the existing theory on coarsening in a granular gas.

Part I

Leidenfrost Effect in a Granular Gas

Chapter 2

Granular Leidenfrost Effect: Experiments

2.1 Original Leidenfrost Effect

The "Leidenfrost effect" was first reported by Hermann Boerhaave in 1732, but not investigated thoroughly until Johann Gottlob Leidenfrost published "A Tract About Some Qualities of Common Water" in 1756, which was not translated from Latin until 1966 [7]. This effect can be observed when a droplet of water impinges on a hot surface, where the droplet sometimes survives for an astonishingly long time.
Leidenfrost himself performed the experiments with an iron spoon heated red-hot in a fireplace as sketched in Fig. 2.1. He carefully put a drop of water into the spoon and timed (with a pendulum) how long the drop survived. On the spot where the drop had been, the spoon turned dull, but the surroundings were still red-hot. After depositing the first drop, he noticed the survival time of the next drops decreased rapidly. The explanation for this

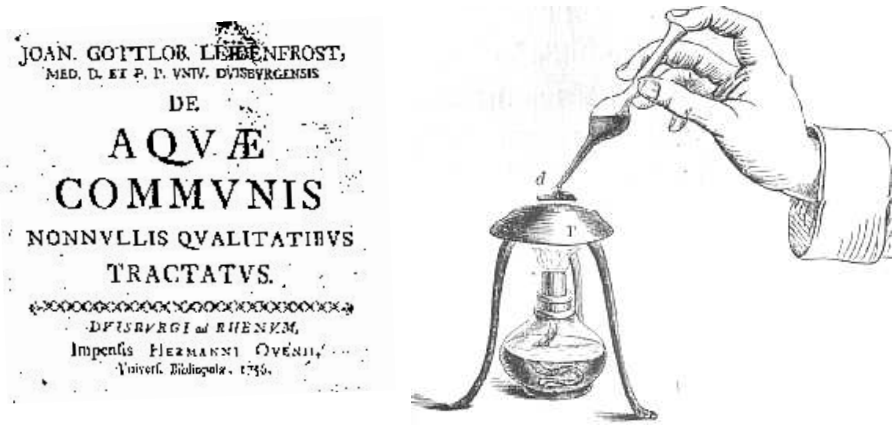

Figure 2.1: A sketch of the authentic setup used by Johann Gottlob Leidenfrost around 1756 for the experiments nowadays associated with his name (from [8]).

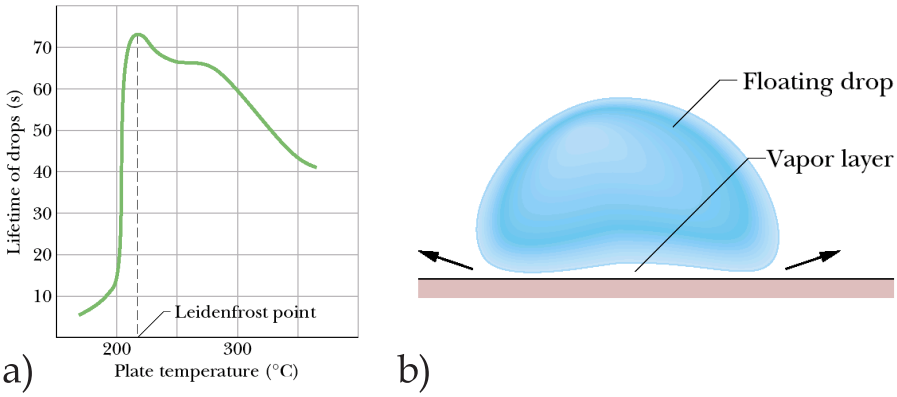

Figure 2.2: a) The lifetimes of drops of distilled water on a hot plate for various plate temperatures shows a remarkable high peak at the Leidenfrost point and it can be explained by b) a sketch of the cross section of a surviving drop of water on a hot plate. The vapor layer prevents direct heat transfer from the hot surface to the surviving drop (from [9]).

phenomenon is that above a certain temperature, the Leidenfrost point (above the boiling point of the droplet-liquid), the bottom layer of the droplet produces vapor immediately after touching the hot surface, see Fig. 2.2 [9]. This vapor-cushion is constantly fuelled by the droplet and prevents it from touching the hot surface, so no heat transfer can take place directly from the hot surface to the droplet. Indirectly there is still heat transfer possible through the vapor-layer, but water vapor is a poor conductor. So just a little heat can be transferred indirectly, which explains the long survival of the water droplet on a very hot surface as can be seen in the graph of Fig. 2.2. The Leidenfrost point of water is $T_L \approx 220\,^{\circ}\mathrm{C}$ depending on the circumstances and the effect is much more pronounced when distilled water is used. When the temperature of the hot surface is below the Leidenfrost point, but well above the boiling temperature, a droplet of water will spread out and vaporize in a few moments. As a result of this spreading the drop quickly absorbs so much energy it instantly vaporizes [10].

A granular version of the Leidenfrost effect was first observed in a Discrete Element Method simulation by Lan and Rosato [11], and more recently in a Molecular Dynamics (MD) simulation by Meerson et al. [12]. This report handles the first experimental evidence of the Granular Leidenfrost effect, in a quasi-2D container. When the container is vertically vibrated above a critical shaking strength, and for a sufficient number of particles, a crystal-like cluster of particles is elevated and supported by a few fast particles underneath the cluster. The cluster shows an almost perfect hexagonal close packing, causing the density to be maximal at the floating cluster. Near the vibrating bottom and above the cluster the density is distinctively lower. This means that the particles are moving faster, so the granular temperature below and above the cluster is higher than in the cluster itself. Thus, this is the granular version of the Leidenfrost effect.

2.2 Experimental Setup

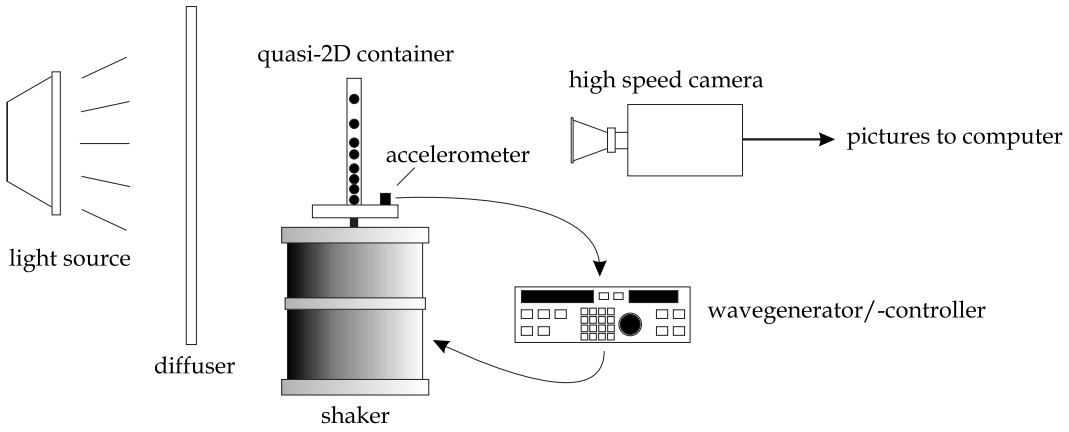

Figure 2.3: Sketch of the setup used for the Granular Leidenfrost effect experiments.

A sketch of the setup for the Granular Leidenfrost effect is depicted in Fig. 2.3. The main point of the setup is the perspex, poly(methylmethacrylaat) or PMMA, container holding the glass beads of diameter $d = 4.0mm$ and density $\rho = 2.5g/cm^3$. The glass beads are sufficiently large to safely neglect the role of the interstitial air.
The depth of the quasi-2D container is a little larger than the diameter of the glass beads ($d_{container} = 4.5mm$) such that the beads can move in a vertical plane without jamming the container.
All experiments have been recorded with a high-speed camera (see appendix A for the specifications of all the equipment used). The camera recorded at 1000 frames per second, so a very intense light source was used to get bright pictures in the short exposure time ($< 1ms$). A diffusive plate was used to diffuse the light for better quality pictures. Before recording each experiment the setup had to be in a steady state, after which the camera was triggered and typically the first 300 consecutive pictures were saved to a computer. The snapshot of Fig. 2.4 was made of a typical experiment using a Digital Video camera at a rate of 25 frames per second.

The shaker is controlled by the wavegenerator with amplifier and the actual amplitude and frequency of the shaker is checked by the accelerometer. The accelerometer signal is then fed back to the wavegenerator/-controller in order to maintain the frequency and amplitude. The amplitude range was typically $a = 0.1 - 5.0mm$ and the shaking frequency was varied from $f = 10 - 200Hz$.
The exact container width is $L_x = 10.04cm$, which means that 25 glass beads fit neatly in a row on the bottom of the container without jamming it. In order to get to the lowest energetic packing, the next row of beads naturally shifts half a bead. In this way every two layers contain 49 beads of $d = 4.0mm$. The number of layers in the container varied from $F = 1$ to $F = 20$ layers. A picture of the setup with the shaker and container is shown in Fig. 2.5.

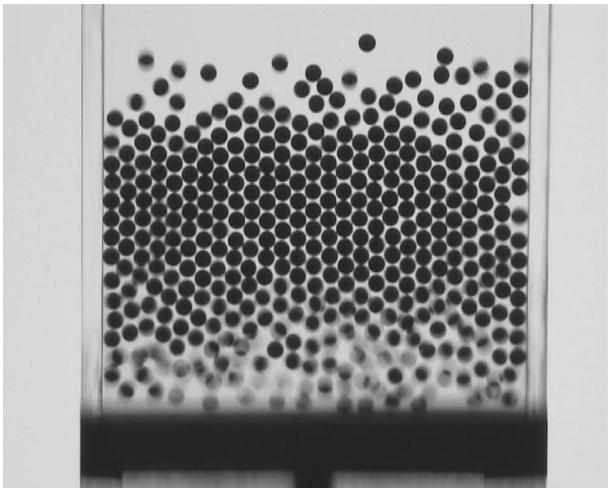

Figure 2.4: Typical experimental snapshot made with a Digital Video camera (at 25 frames per second) for $F = 16$ layers of glass beads shaken with an amplitude of $a = 4.0mm$ and at a frequency of $f = 90Hz$.

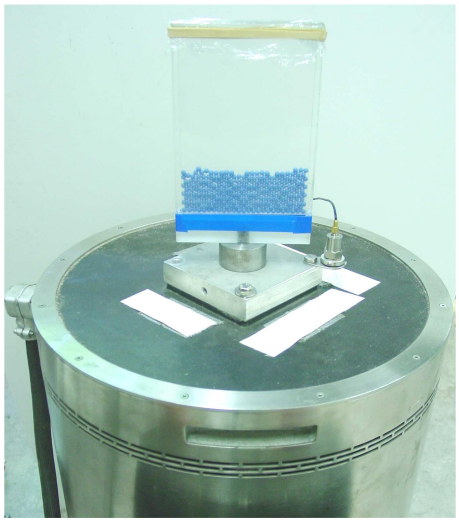

Figure 2.5: The quasi-2D container with glass beads, mounted on the shaker.

As mentioned already in section 1.2 the glass beads are acting as a granular gas when shaken vigorously. These particles exhibit a special feature compared to ordinary gases: the collisions are inelastic, i.e. the normal restitution coefficient is $e < 1$. This means that only the momentum is conserved in each collision, but that some of the energy is dissipated (momentum and energy are both preserved for elastic collisions, $e = 1$).

2.3 Experimental Observations

The parameters that have been changed independently during the experiments were the number of layers F, the amplitude a and the frequency f. By changing the amplitude and the frequency, the dimensionless shaking strength Γ is changed,

$$\Gamma = \frac{a(2\pi f)^2}{g}. \tag{2.1}$$

Above a certain critical shaking strength Γ_c, the Granular Leidenfrost effect can be observed provided that the system contains sufficiently enough glass beads. Three typical experimental pictures recorded with the high-speed camera using 16 layers of beads for increasing shaking strength can be seen in Fig. 2.6. The fact that the Granular Leidenfrost effect, or vertical clustering, occurs towards stronger shaking is remarkable, since in all other granular cluster experiments the clustered state is reached when the shaking strength is decreased [13]!

The Granular Leidenfrost effect can be observed only for a sufficient number of layers, see Fig. 2.7.The minimum number of layers for which the Granular Leidenfrost effect can be observed in the performed experiments is around $F = 10$. The existence of a minimum means that the effect can be triggered by adding particles to the system.

One problem we had to deal with in the experiment was the fact that static electricity was building up during shaking. Static electricity develops when two different non-conducting materials come into contact with each other and by adhesion a chemical bond is formed. In contact, one material can capture some electrons from the other and when the materials are then separated, one material is negatively charged and the other positively.

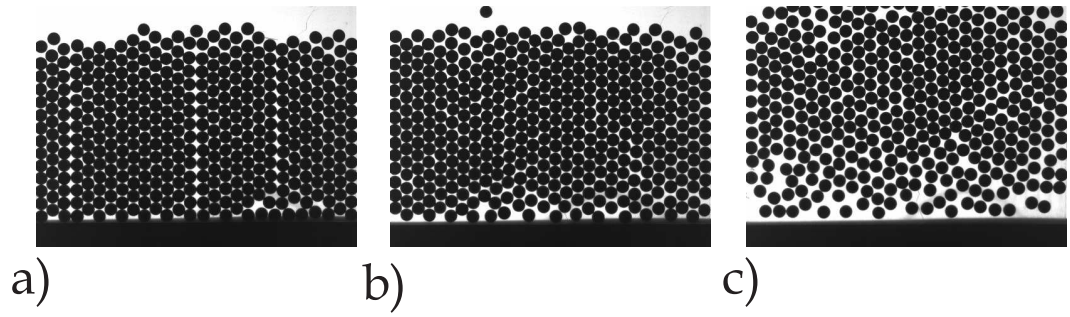

Figure 2.6: Three typical experimental pictures made with a high-speed camera at 1000 fps for $F = 16$ layers of glass beads with different shaking strengths are shown here: a) The top of the pile is just about to fluidize at $\Gamma = 7.7$ ($f = 80Hz$ and $a = 0.3mm$). b) At a shaking strength of $\Gamma = 25.8$, just above Γ_c, the system is clearly above the fluidization point ($f = 80Hz$ and $a = 1.0mm$). Larger shaking strengths will develop a more pronounced inversion than the one displayed here. c) For vigorous shaking at $\Gamma = 51.5$ a clear density inverted state is present ($f = 80Hz$ and $a = 2.0mm$).

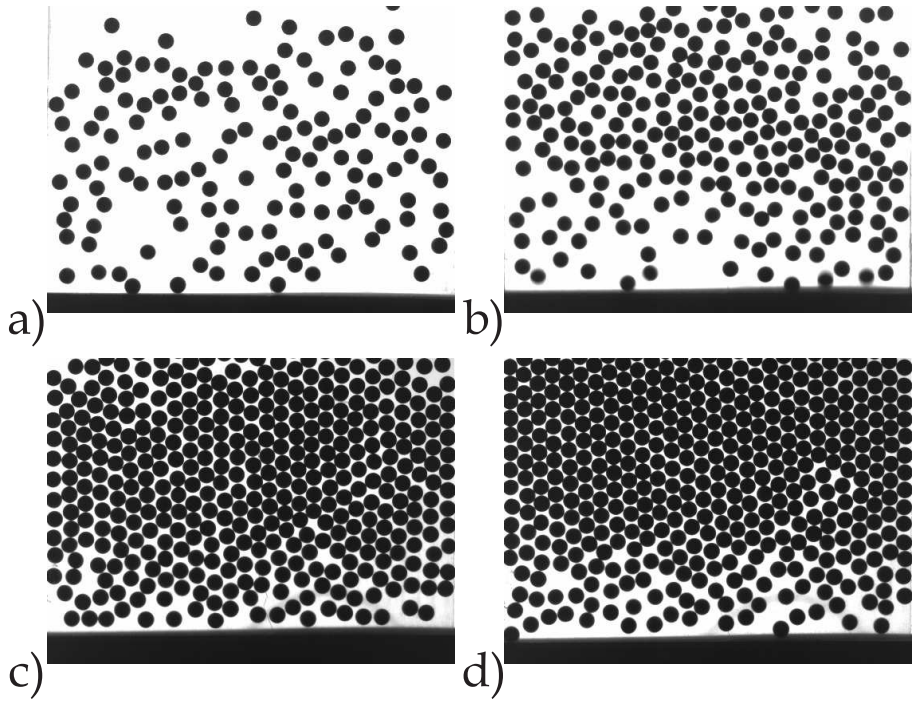

Figure 2.7: The changing behavior of the glass beads in the vigorously shaking quasi-2D container can be observed in experiments with different number of layers: a) No Granular Leidenfrost effect is present for $F = 6$ layers shaken at $\Gamma = 51.5$ ($f = 80Hz$ and $a = 2.0mm$). b) At a shaking strength $\Gamma = 81.5$ for $F = 10$ layers the effect just exists ($f = 90Hz$ and $a = 2.5mm$). c) A density inverted state is clearly observed using $F = 16$ layers shaken at $\Gamma = 51.5$ ($f = 80Hz$ and $a = 2.0mm$) d) and it is even more pronounced for $F = 20$ layers with $\Gamma = 65.2$ ($f = 90Hz$ and $a = 2.0mm$).

This static electricity depends on the combination of materials and to be exact, it depends on the relative position in the triboelectric series [14]. For example, the glass beads will get positively charged when rubbed against the shaking perspex container. Accordingly, this charge imbalance will attract the glass beads to the perspex walls of the container, which will affect the results of the experiments to some unknown extent.
In order to prevent static electricity in the Granular Leidenfrost effect experiments, the humidity was kept constant and as high as possible using an air-conditioner. A high humidity supplies a small coat of moisture on the surface of the material, in this way providing an easy path for the electrons to neutralize the charge imbalance. Before recording an experiment the static electricity was checked and when it was observed, the container was opened to "breathe" or sometimes even emptied out to stop the static electricity building up.

2.4 Data Processing

The sequences of experimental high-speed pictures, of which some typical examples were shown in section 2.3, are then automatically and identically analyzed with digital image processing. All pictures have the same size of 512x384 pixels and the view of the high-speed camera covered exactly the inner width of the container without recording the sidewalls. So, without a problem the pictures could be analyzed immediately after recording by just counting the number of black pixels, i.e. the pixels belonging to the beads, in each row. When this number of bead pixels is divided by the total number of pixels in a row, 512, the solid fraction ρ is obtained for this particular row. The solid fraction is determined for all 384 rows in each picture, whereafter all values for every row are averaged over all recorded pictures. See the solid fraction plot for the example experiment of $F = 16$ layers shaken at $f = 80Hz$ and amplitude $a = 2.0mm$ ($\Gamma = 51.5$) in Fig. 2.8. From the solid fraction plot it should be noted that the origin of the height ($h = 0$) is chosen to be at the maximal positive displacement of the vibrating bottom in all experiments. In theoretical models for simplicity the bottom is commonly considered to be stationary as proposed by Eggers [15]. So this choice for the origin facilitates the comparison between experiments and theory. Another advantage of this choice is that for the shaking parameters a and f the same reference frame is used.

The height h is made dimensionless by dividing it by the bead diameter d, which is measured in pixels in each experiment. The bead diameter is known ($d = 4.0mm$), so in this way the resolution of every experiment is determined and the dimensionless height h/d can be constructed.
The result of Fig. 2.8 is strikingly different from the standard barometric height distribution

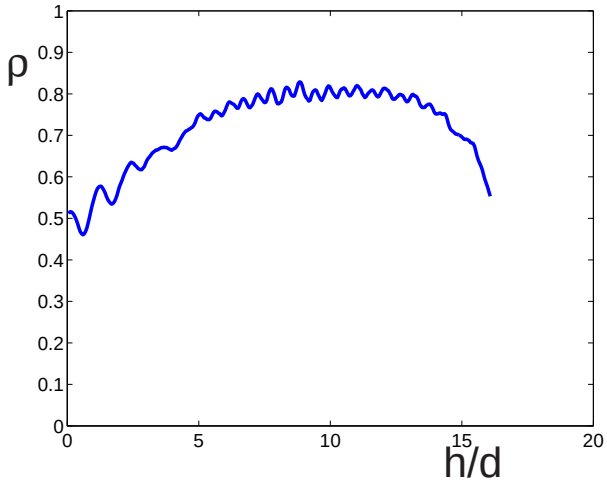

Figure 2.8: The unprocessed solid fraction ρ (averaged over 300 experimental pictures) measured as a function of the dimensionless height h/d for $F = 16$ layers. Shaking parameters: $a = 2.0mm$ and $f = 80Hz$, corresponding to $\Gamma = 51.5$.

known for ideal gases. In an ideal granular gas, the particles obey the equation of state:

$$p = nk_BT, \tag{2.2}$$

i.e. the ideal gas law, where p is the pressure, n the number density, $k_B = 1.38 \cdot 10^{-23} J/K$ Boltzmann's constant and T the granular temperature. The granular particles also have to comply with the momentum balance,

$$\frac{dp}{dz} = -mgn, \tag{2.3}$$

in which $-mg$ depicts the gravitational force with gravitational acceleration g on a single particle mass m. If the granular temperature T is assumed to be independent of the height z, these equations combine to $k_BTdn/dz = -mgn$, what leads to the barometric height formula:

$$n(z) = n(0)e^{-mgz/k_BT}. \tag{2.4}$$

Instead of this exponentially decaying number density the Granular Leidenfrost experiments show a clear density inversion.

Simultaneously with the determination of the solid fraction, the motion of the bottom is tracked also in the recorded sequences and together with the known resolution, the amplitude and frequency can be reconstructed. The frequency entered on the wavegenerator/-controller always agrees perfectly with the actual frequency. The actual amplitude is systematically just a little higher (maximal 5%) than entered, so it is permitted to neglect this deviation.

The averaged solid fraction plot of Fig. 2.8 needs to be smoothed in order to determine the inversion height h_{inv}, because a higher order polynomial fit did not work properly for all experiments. In the experiments with a small or no inversion, the inversion height was not determined correctly. So, the solid fraction needed to be smoothed using a running average in which a certain number of data points before and after the initial data point is averaged and assigned to that point. Problems with this averaging method occurred for the first and last couple of points, because of the lack of data points before or after the point of interest. This was solved by simply extrapolating these first and last couple of points.
From this smoothed solid fraction plot the derivative could easily be taken with the perspective of determining the inversion height as the height for which the derivative is zero for the first time. Besides this inversion height h_{inv}, the height for maximal solid fraction h_{max} and the height with last zero-derivative h_{top} have been determined for all experiments. The resulting plots for the example experiment of $F = 16$ are depicted in Fig. 2.9. The values for h_{inv} and h_{top} can be regarded as the lower and upper boundary of the crystal-like structure in the original experimental picture. From Fig. 2.10 it may be observed that the relation $h_{max} = \frac{h_{inv}+h_{top}}{2}$ holds on the average.

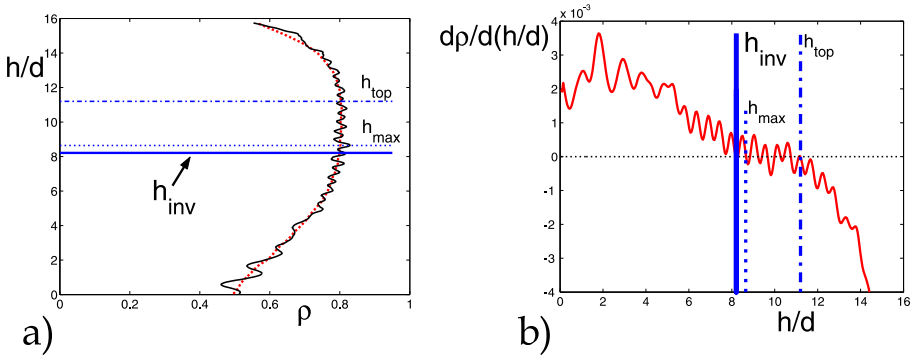

Figure 2.9: a) The original solid fraction (black solid) is processed by the running average method producing the smoothed solid fraction plot (red dotted). b) The derivative of this smoothed curve (red solid) defines the inversion height $h_{inv} = 8.2$ (blue solid) by the determination the first height with zero derivative. In the same way $h_{top} = 11.2$ (blue dash-dotted) is determined, being the last zero derivative and the maximal achieved solid fraction $h_{max} = 8.6$ (blue dotted). Shaking parameters: $F = 16$, $a = 2.0mm$ and $f = 80Hz$, corresponding to a shaking strength $\Gamma = 51.5$.

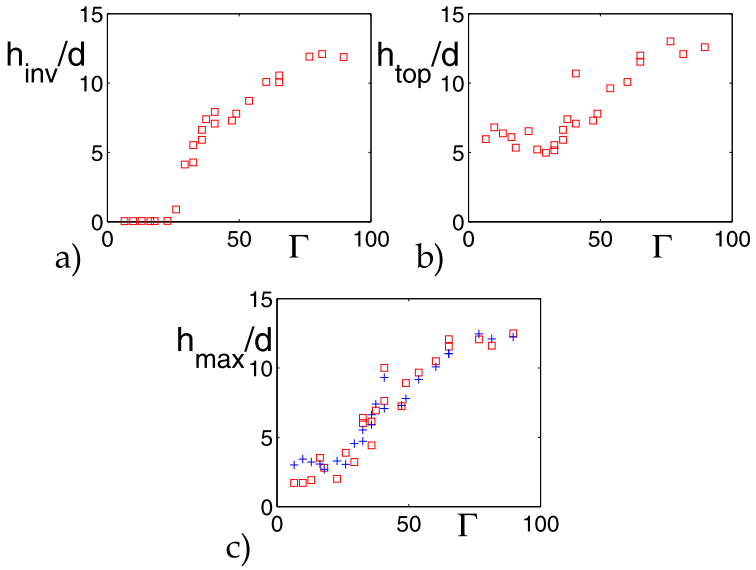

Figure 2.10: $F = 10$ layers shaken with different amplitudes a for a fixed frequency $f = 90Hz$. a) As a function of shaking strength, the inversion height h_{inv} and b) the upper boundary of the piston h_{top} are shown. c) Evidence of the relation $h_{max} = \frac{h_{inv}+h_{top}}{2}$, i.e. that h_{max} (red squares) and $(h_{inv} + h_{top})/2$ (blue plus signs) are the same on the average.

Chapter 3

Granular Leidenfrost Effect: Theory

3.1 Basic Equations

To describe the Granular Leidenfrost effect in a 2D situation the hydrodynamic steady state equations, for instance used by Grossman et al. [16], Eggers [15] and Meerson et al. [12], can be used for a continuum description;

$$p = nT\frac{n_c + n}{n_c - n}, \qquad n_c = \frac{2}{\sqrt{3}d^2} \tag{3.1}$$

$$\frac{dp}{dz} = -mgn \tag{3.2}$$

$$\frac{d}{dz}\{\kappa T^{1/2}\frac{dT}{dz}\} = \lambda n^2 T^{3/2} \tag{3.3}$$

Equation (3.1) is the equation of state for $k_B = 1$ with the finite volume effect incorporated. Here $p(z)$ is the pressure, $n(z)$ the number density and T the granular temperature: $T \propto m\langle v^2\rangle$ (m is the mass of a single particle). The height z is measured from the bottom of the container and n_c is the maximal number density in two dimensions for particles of diameter d in a hexagonal close packing. The second equation (3.2), is the force balance with the force on a single particle being $-mg$. The third equation shows the energy balance of the heat flux through the system and the dissipation due to particle collisions. The thermal conductivity is proportional to the average particle velocity $\langle v\rangle$, hence the term $\kappa T^{1/2}$ on the left hand side of (3.3). The dissipation term (right hand side) emerges from the energy loss in one collision $(1 - e^2)T$ and the total number of collisions, which is proportional to $n^2 v \propto n^2 T^{1/2}$, yielding the total energy dissipated by all inelastic collisions $\propto n^2 T^{3/2}$. The coefficients κ and λ for 2D circular disks of diameter d have been found by Jenkins and Richman [17]: the thermal conductivity coefficient is equal to $\kappa = \frac{2m}{\sqrt{\pi}d}$ and the dissipation coefficient is determined to be $\lambda = 2\sqrt{\pi}md(1 - e^2)$.

To solve this set of three equations, three boundary conditions are required of which a constant granular temperature at the bottom is the first one:

$$T(z = 0) = T_0 = mv_{bottom} = m(af)^2 = constant. \tag{3.4}$$

In this way a constant energy supply is provided at the bottom, which is shaking at an amplitude a and frequency f. The second boundary condition is a zero heat flux at the top, thus a constant granular temperature at $z \to \infty$:

$$\left.\frac{dT}{dz}\right|_{z\to\infty} = 0. \tag{3.5}$$

The third boundary condition is the conservation of the total number of particles N,

$$\int_0^\infty n(z)\,dz = N/L_x = F d n_c = constant. \tag{3.6}$$

3.2 Dimension Analysis

To analyze the set of equations (3.1-3.3), they can be made dimensionless by means of:

$$z \;\mapsto\; \widetilde{z} = \frac{z}{d}, \tag{3.7}$$

$$n \;\mapsto\; \widetilde{n} = \frac{n}{n_c}, \tag{3.8}$$

$$T \;\mapsto\; \widetilde{T} = \frac{T}{T_0}. \tag{3.9}$$

Applying these three dimensionless parameters to the set of hydrodynamic equations yields:

$$p = (n_c T_0)\widetilde{n}\widetilde{T}\frac{1+\widetilde{n}}{1-\widetilde{n}}, \tag{3.10}$$

$$\frac{dp}{d\widetilde{z}} = -(mgdn_c)\widetilde{n}, \tag{3.11}$$

$$\frac{d}{d\widetilde{z}}\{\kappa\widetilde{T}^{1/2}\frac{d\widetilde{T}}{d\widetilde{z}}\} = (dn_c)^2\lambda\widetilde{n}^2\widetilde{T}^{3/2}. \tag{3.12}$$

By inserting (3.10) into (3.11), the pressure p can be eliminated, leaving a set of two equations:

$$\frac{d}{d\widetilde{z}}\{\widetilde{n}\widetilde{T}\frac{1+\widetilde{n}}{1-\widetilde{n}}\} = -\{\frac{mgd}{T_0}\}\widetilde{n}, \tag{3.13}$$

$$\frac{d}{d\widetilde{z}}\{\widetilde{T}^{1/2}\frac{d\widetilde{T}}{d\widetilde{z}}\} = \pi(d^2n_c)^2(1-e^2)\widetilde{n}^2\widetilde{T}^{3/2}. \tag{3.14}$$

In (3.14) is made use of the relation between the dissipation coefficient λ, and the coefficient κ for the thermal conductivity: $\lambda/\kappa = \pi d^2(1-e^2)$.
In order to describe the Granular Leidenfrost experiments with this continuum model, the

next four dimensionless control parameters can be defined:

$$\Gamma = \frac{a(2\pi f)^2}{g} \tag{3.15}$$

$$F = \frac{h}{d} \tag{3.16}$$

$$A = \frac{a}{d} \tag{3.17}$$

$$\epsilon = (1 - e^2) \tag{3.18}$$

Where Γ is the dimensionless shaking strength, F the filling height, A the dimensionless shaking amplitude and ϵ the inelasticity of the granular particles. Using these four control parameters, the hydrodynamic equations (3.13, 3.14) will be solved in the next section.

3.3 Solving the Theoretical Model

To numerically solve the set of equations (3.13, 3.14), they can be rewritten using the dimensionless control parameters:

$$\frac{d}{d\widetilde{z}}\{\widetilde{n}\widetilde{T}\frac{1+\widetilde{n}}{1-\widetilde{n}}\} = -\frac{1}{S}\widetilde{n}, \qquad S = \Gamma A, \tag{3.19}$$

$$\frac{d\widetilde{T}^{3/2}}{d\widetilde{z}^2} = 2\pi\epsilon\widetilde{n}^2\widetilde{T}^{3/2}. \tag{3.20}$$

In equation (3.19) the term (mgd/T_0) is rewritten in terms of $S = \Gamma A$ using the definition of T_0 (3.4). Based on the three boundary conditions discussed in section 3.1, the next dimensionless boundary conditions can be defined:

$$\widetilde{T}_0 = 1, \tag{3.21}$$

$$\left.\frac{d\widetilde{T}}{d\widetilde{z}}\right|_{\widetilde{z}\to\infty} = 0, \tag{3.22}$$

$$\int_0^\infty \widetilde{n}(\widetilde{z})\, d\widetilde{z} = F. \tag{3.23}$$

Note that in the set of dimensionless hydrodynamic equations with the corresponding dimensionless boundary conditions (3.19)-(3.23), all the dimensionless control parameters defined in section 3.2 emerge. So, these four parameters (Γ, F, A and ϵ) are indeed the control parameters for this system described by the hydrodynamic equations.

In order to solve this set of dimensionless equations, the next three (also dimensionless) parameters are defined:

$$U = \widetilde{T}^{3/2}, \tag{3.24}$$

$$V = \frac{d}{d\widetilde{z}}(\widetilde{T}^{3/2}) = \frac{dU}{d\widetilde{z}}, \tag{3.25}$$

$$W = \widetilde{n}. \tag{3.26}$$

These parameters can be used to form the next three first-order equations based on (3.19, 3.20):

$$\frac{dU}{d\widetilde{z}} = V, \tag{3.27}$$

$$\frac{dV}{d\widetilde{z}} = 2\pi\epsilon W^2 U, \tag{3.28}$$

$$\frac{d}{d\widetilde{z}}\{WU^{2/3}\frac{1+W}{1-W}\} = -\frac{1}{S}W. \tag{3.29}$$

Here, equation (3.27) directly comes from the definition for the dimensionless parameter V (3.25). To proceed equation (3.29) can be differentiated with respect to $\widetilde{z}$, leading to the final set of input equations to solve the model numerically with this continuum model:

$$\frac{dU}{d\widetilde{z}} = V, \tag{3.30}$$

$$\frac{dV}{d\widetilde{z}} = 2\pi\epsilon W^2 U, \tag{3.31}$$

$$\frac{dW}{d\widetilde{z}} = W\frac{-\frac{1}{S}(1-W)^2 - \frac{2}{3}(1-W^2)U^{-1/3}V}{U^{2/3}(-W^2+2W+1)}. \tag{3.32}$$

The three dimensionless boundary conditions mentioned above, can be rewritten using the parameters U, V and W to solve the model with an ODE-solver (Ordinary Differential Equation):

$$U(0) = \widetilde{T}^{3/2}(0) = 1, \tag{3.33}$$

$$V(\widetilde{z}\to\infty) = 0, \tag{3.34}$$

$$W(0) = -\frac{1+\frac{F}{S}}{2} + \frac{\sqrt{(1+\frac{F}{S})^2+4\frac{F}{S}}}{2}. \tag{3.35}$$

The first boundary condition is straightforward, the dimensionless temperature has to be constant at the bottom. Furthermore, a zero heat flux at the top is the second boundary condition and the last condition is derived from the conservation of the total number of particles, see (3.6), which reads:

$$\int_0^\infty W d\widetilde{z} = F. \tag{3.36}$$

The boundary condition for $W(0)$, equation (3.35), is found if this conservation integral is used when integrating equation (3.29).

The second boundary condition (3.34) is not fulfilled at once, because it depends on the initial value of $V(0)$:

$$V(0) = \frac{3}{2}\frac{d\widetilde{T}}{d\widetilde{z}}\bigg|_{\widetilde{z}=0} = -t \leq 0. \tag{3.37}$$

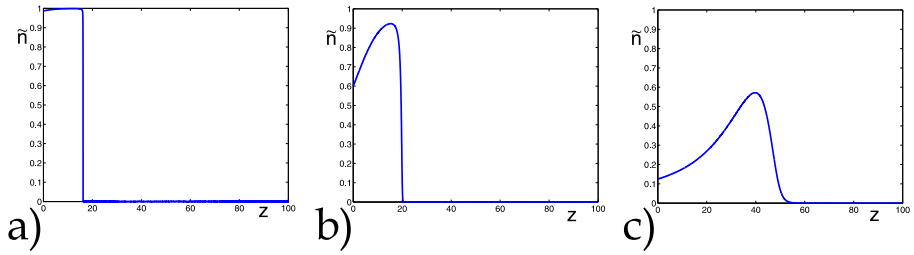

Figure 3.1: The dimensionless number density $W = \widetilde{n} = n/n_c$ as a function of the height z for $F = 16$ layers. a) At a low shaking strength ($S = 0.11$) the continuum model shows a typical number density plot of a system almost at rest. b) If the system is shaken stronger ($S = 6.67$) a density inversion is starting to build up and c) for vigorous shaking ($S = 100$) the Granular Leidenfrost effect can be clearly observed in the theoretical density profile.

Unfortunately no a priori knowledge is available about the behavior of V at the bottom. Logically the slope of the granular temperature curve will be smaller than (or equal to) zero, because dissipation will decrease the granular temperature above the bottom. The shooting method is used to provide that $V(\widetilde{z} \to \infty)$ is sufficiently close to zero. This method means that the shooting parameter t is varied up and down, depending on the outcome of the condition for V (3.34), until this condition is met [18]. Then all boundary conditions are fulfilled and the ODE-solver can calculate the final profiles for U, V and W. A typical development of the resulting dimensionless number density W for $F = 16$ layers is shown in Fig. 3.1. From Fig. 3.1 it can be concluded that the continuum model successfully describes the Granular Leidenfrost effect qualitatively. However, the experimentally observed phenomenon of a constant density plateau for a sufficient number of layers is not found in the theoretical results for the number density.
Fig. 3.2 shows the plots for $U = \widetilde{T}^{3/2}$ and $V = \frac{d}{d\widetilde{z}}(\widetilde{T}^{3/2}) = \frac{dU}{d\widetilde{z}}$ corresponding to Fig. 3.1c). It may be noted that when the condition $V(\widetilde{z} \to \infty) = 0$ was fulfilled, this condition was always at the border of getting imaginary.

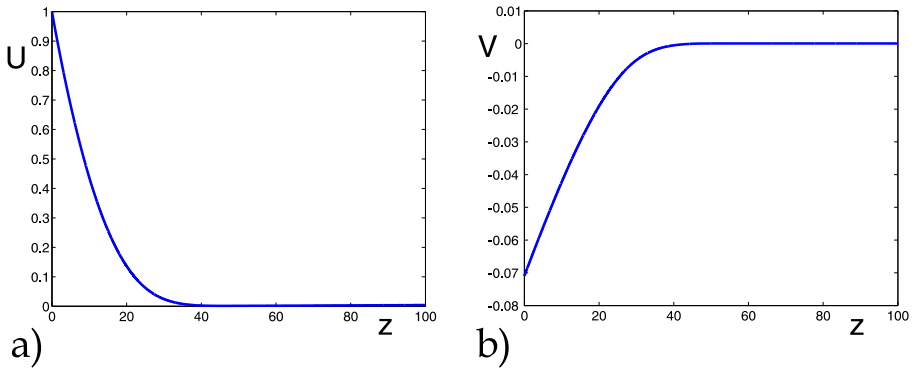

Figure 3.2: a) $U = \widetilde{T}^{3/2}$ versus z for $F = 16$ at vigorous shaking of $S = 100$, corresponding to Fig. 3.1c). b) $V = \frac{dU}{d\widetilde{z}}$ as a function of height for the same case.

Chapter 4

Granular Leidenfrost Effect: Experiment vs. Theory

4.1 Second Order Phase Transition

First order phase transitions are associated with the coexistence of two distinct phases, like in boiling water, where both the liquid and the gas phase are present. In a second order phase transition, the transitions are continuous without the coexistence of two phases at any point. Consider for example, the ferromagnetic second order phase transition of iron: the magnetization increases continuously from zero as the temperature is lowered below the Curie temperature T_C.
In the granular Leidenfrost experiments a second order phase transition can be observed, when the inversion height is considered. In Fig. 4.1 the determination of the inversion height h_{inv} is shown again.

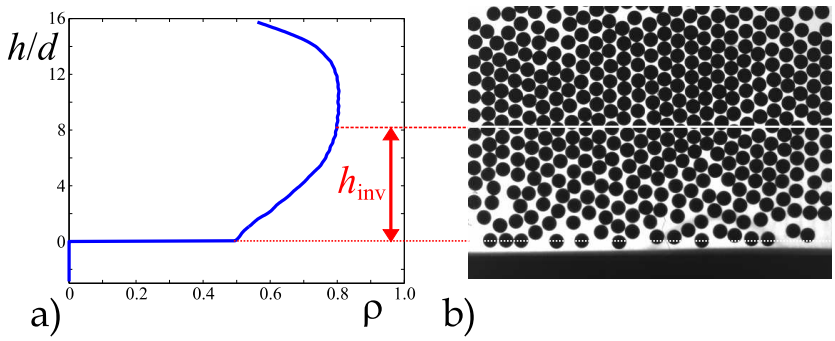

Figure 4.1: a) The smoothed solid fraction plot with the determined inversion height h_{inv} of b) the original experimental picture of the experiment performed with $F = 16$ layers at a shaking strength of $\Gamma = 51.5$ ($f = 80Hz$ and $a = 2.0mm$).

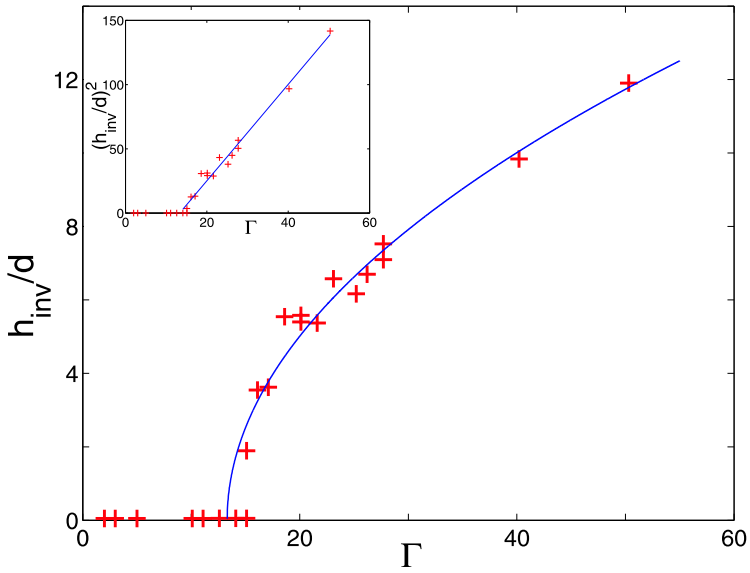

Figure 4.2: The inversion height h_{inv} for $F = 10$ layers as a function of the shaking strength Γ (frequency fixed at $f = 50HZ$). It shows a continuous second order phase transition at the critical shaking strength $\Gamma_c = 15$. The squared inversion height h_{inv}^2 plot (inset) demonstrates a straight line above the transition, so: $h_{inv} \propto (\Gamma - \Gamma_c)^{1/2}$.

In a sequence of experiments with $F = 10$ layers of glass beads at a fixed frequency $f = 50Hz$ the phase transition plot of Fig. 4.2 was constructed. Fig. 4.2 clearly fulfills the conditions of a second order phase transition to develop without discontinuities and without the existence of two distinct phases at the same time. The transition starts at the critical shaking strength Γ_c, which is determined by taking the Γ corresponding to the first nonzero inversion height. The inset shows a linear relation between the squared inversion height and the shaking strength. So beyond the critical shaking strength, the inversion height grows as $h_{inv} \propto (\Gamma - \Gamma_c)^{\beta}$, with the mean field exponent $\beta = 1/2$.
Experimental proof has been provided that no hysteresis is present in the Granular Leidenfrost experiments: Normally the steady state is reached from a starting point without shaking, but the experiments to check the hysteretic effect started at a shaking strength of $\Gamma = 90$ and then lowered to the desired Γ. The results of these experiments completely match the other experiments, so no hysteretic effect is present here.
For five experiments with $F = 10$ layers the second order phase transition plot of h_{inv} has been determined. From these plots an estimate for the errorbar of h_{inv} was determined, being typically 5 to 10%.

The continuum model results for the number density show inversion for all shaking strength if the number of layers is $F > 3$, so even in Fig. 3.1a) an inversion is found if the inversion height is determined in the same way as in the experiments (the height with first zero derivative). Therefore, the inversion height in the continuum model has alternatively

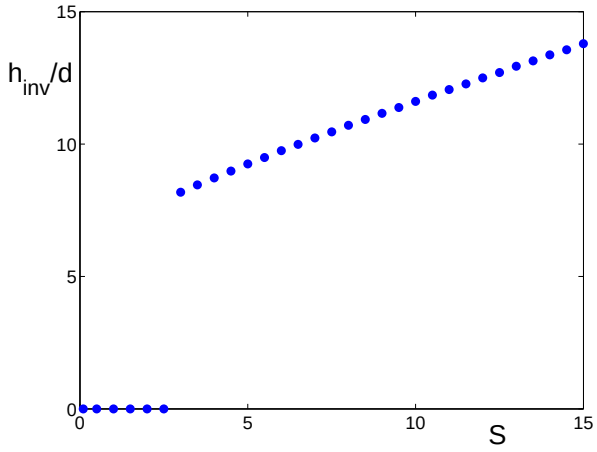

Figure 4.3: Inversion height h_{inv} as a function of shaking strength S determined by the continuum model for $F = 16$ layers.

been determined using a threshold for the n-value at $\widetilde{z} = 0$. This threshold value is adopted from the minimal number density ($n_{min} = 0.68$) for an ideal hexagonal close packing. If the density profile has a larger value than $n(0) = 0.68$ it is considered to exhibit *no* inversion. For $n(0)$-values below this threshold, the inversion height is again the height for which the derivative is zero for the first time. Other choices of this threshold value will just change the critical shaking strength after which inversion can be observed in the theoretical model. Fig. 4.3 shows the corresponding inversion height plot for $F = 16$ layers obtained by solving the set of equations using the shooting method as described in section 3.3. This plot resembles the one of Fig. 4.2, but this time the transition is discontinuous.

In short it can be concluded that the continuum model does describe the Granular Leidenfrost effect qualitatively with respect to the the density profiles, but no second order phase transition is found for the theoretical model. The reason for this different behavior compared to the experimental observations has to be searched for in the definition for κ and λ in section 3.1. Grossman et al. [16] and Meerson et al. [12] used for the coefficients of thermal conductivity and dissipation the following relations:

$$\kappa \propto \frac{n(\alpha l + d^2)T^{1/2}}{l}, \qquad l = \frac{1}{\sqrt{8}nd}\frac{n_c - n}{n_c - an}, \tag{4.1}$$

$$\lambda \propto \frac{(1 - e^2)}{l}. \tag{4.2}$$

Here l is the mean free path and the constant a is determined to be $a = 1 - \sqrt{3/8}$ for a two-dimensional packing. The resulting density profiles show a density inverted state *plus* the extra feature of a plateau of constant number density [12]. The current continuum model should be adapted using these new relations (4.1, 4.2) in order to investigate the experimentally observed second order phase transition for the inversion height h_{inv}.

Another important aspect which is not included in the model at the moment, is the effect of the walls of the quasi-2D container. The glass beads are continually colliding with the side-, front- and back walls, dissipating energy, which is not described by the current continuum model.

4.2 Exploring the Parameter-space

To explore the parameter-space of a, f and F for different number of layers ($F = 1, 3, 5$,-$6, 10, 16, 20$) inversion height plots were constructed. In order to get a density inversion, a sufficiently large number of glass beads is required and from the experiments it has been concluded that the critical number of layers is situated around $F = 10$ layers, see section 2.3. So, for $F \geq 10$ a second order phase transition plot like the one in Fig. 4.2, could be constructed. From each transition plot the critical shaking strength Γ_c was determined and the corresponding critical amplitude a and frequency f are displayed in Fig. 4.4. The results shown in Fig. 4.4 give confidence in $S = \Gamma A \propto (af)^2$ as the important control parameter instead of $\Gamma \propto af^2$, because this graph shows that $\frac{1}{af} = constant$. Thus, at the transition S is constant for all experiments with $F \geq 10$.
The expectation that a higher shaking strength is needed to get to a density inverted state if F is larger was not recovered in Fig. 4.4. It has to be taken into account that the largest number of layers of $F = 20$ is not enormously larger than $F = 10$, where the density inversion can be observed for the first time. Thus, in order to observe a shift to higher shaking strengths the number of layers may have to be increased more.

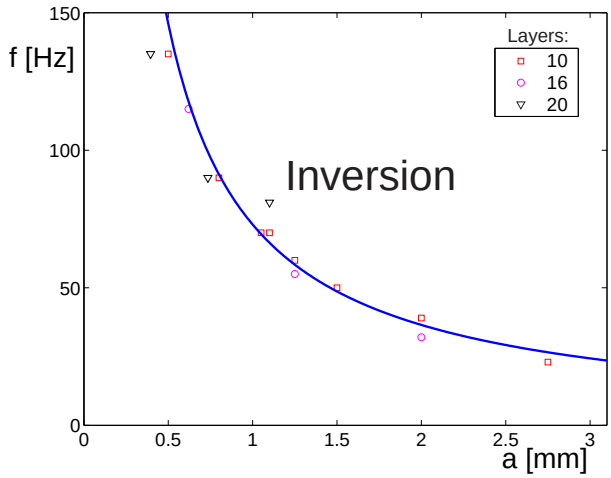

Figure 4.4: For $F \geq 10$ density inversion can be observed above a critical shaking strength Γ_c via a second order phase transition. The corresponding critical amplitude and frequency are plotted for different number of layers. The fit was constructed with the criterion that $\frac{1}{af} = constant$ and above the fit density inversion can be observed in the experiments.

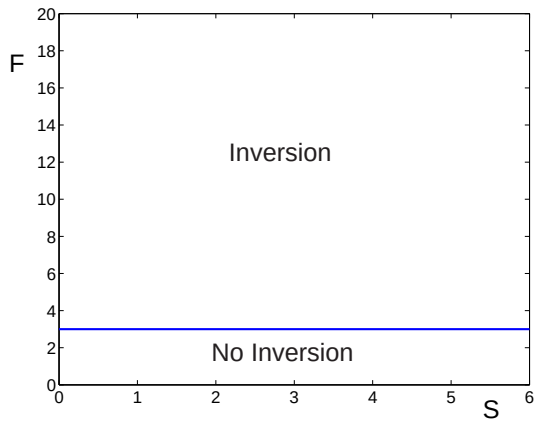

Figure 4.5: The number density results from the continuum model exhibit density inversion for all shaking strengths S if $F > 3$. The corresponding parameter space is depicted here.

The results from the current theoretical model show density inversion for all shaking strengths ($F > 3$) and no inversion for $F \leq 3$. The corresponding parameter space for F and S is shown in Fig. 4.5. Just like in the experiments no inversion at all can be observed if not enough particles are supplied, but there is a difference in the minimal number of layers between the experiment and the model. This may be explained by the simplifications used in the continuum model. When the suggestions of section 4.1 are incorporated, the parameter space of Fig. 4.5 may resemble the experimental one more closely.

Fig. 4.6 shows the parameter space if the threshold for the inversion height discussed in section 4.1 is included. Again, inversion can only be observed in the theoretical model for $F > 3$ and in addition to this, if the number of layers is increased a higher shaking

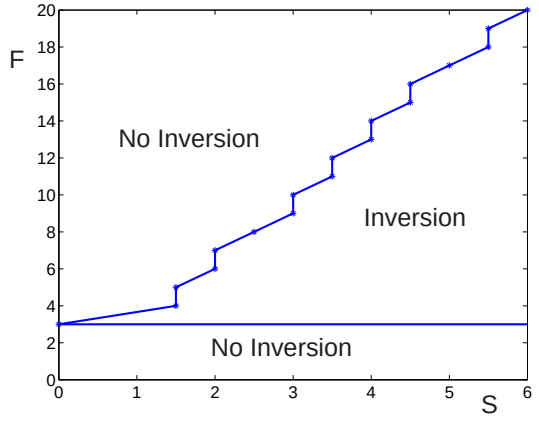

Figure 4.6: If the threshold for the inversion height described in section 4.1 is used, this corresponding parameter space can be constructed. Note that for more layers a higher shaking strength is needed to get inversion.

strength is required to observe inversion. This effect was not observed in the experiments, even though it was expected, as discussed earlier in this section. As a suggestion for future work, the validity of the parameter space of Fig. 4.6 based on the continuum model also has to be checked using the adjustments mentioned in section 4.1.

4.3 Taking the Granular Temperature

The granular temperature defined as $T \propto \langle v^2 \rangle$, can be extracted from the experiments by Particle Tracking Velocimetry (PTV). This method tracks all the particles in every frame and from this information attempts to find out what paths they most likely have followed during all consecutive frames [19]. After processing an experiment with the PTV-method the successive positions are known for almost all particles. From these particle positions the particle velocity $\overrightarrow{v}$ can be determined in every frame, see for an experimental snapshot with corresponding velocity vectors Fig. 4.7. For all frames the velocity values are known and then the absolute velocities can be assigned to the heights of the corresponding glass beads. How the granular temperature typically varies with the height h is demonstrated in Fig. 4.8.

The granular temperature $U^{2/3} = \widetilde{T}$ shown in Fig. 4.9 is determined for $F = 16$ layers shaken vigorously ($S = 100$). This typical temperature profile highly resembles the experimental profile of Fig. 4.8, although the scale along the horizontal axis is quite different. So as far as the temperature is concerned the hydrodynamic continuum model seems to be in qualitative agreement with the experiments performed.

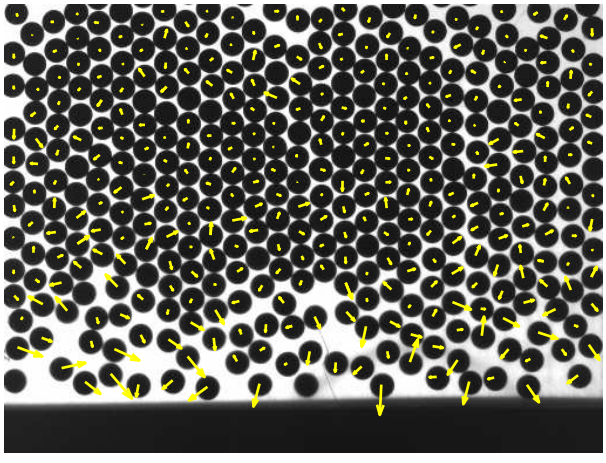

Figure 4.7: An experimental snapshot of an experiment with $F = 16$ layers of glass beads with the corresponding velocity vectors.

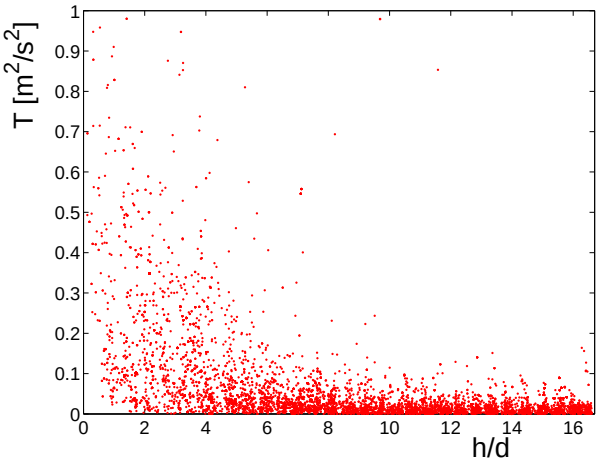

Figure 4.8: The granular temperature $T \propto \langle v^2 \rangle$ as a function of the height h for an experiment with $F = 16$ layers at $f = 90Hz$ and $a = 2.0mm$ (see also Fig. 4.7). The temperature is monotonously decreasing from the vibrating bottom to the cluster. At the top of the cluster, the temperature shows a slight tendency to increase again.

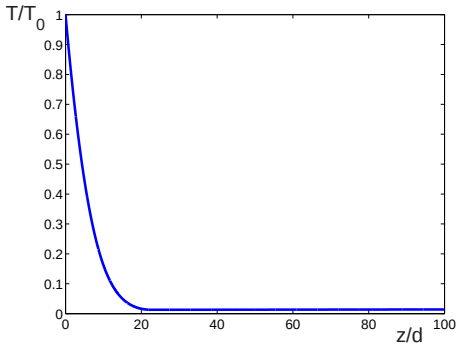

Figure 4.9: The granular temperature $\widetilde{T} = T/T_0 = U^{2/3}$ as a function of the height $\widetilde{z}$ based on the continuum model: $F = 16$ layers at a vigorous shaking strength $S = 100$.

Part II

Coarsening in a Granular Gas

Chapter 5

Coarsening: Introduction

5.1 Coarsening, a ubiquitous phenomenon

Coarsening is the phenomenon observed in the foam of beer for example, where the small foam cells merge into larger ones until the foam only consists of large foam cells. The effect of the large foam cells consuming the smaller ones is called "coarsening" [20], see for example Fig. 5.1.

In granular matter coarsening exists also, for example when a granular material on a circular disk is vertically shaken. Large and small heaps are formed, in which the large heaps eat up the smaller ones, causing the large heaps to grow at the expense of the small heaps, see Fig. 5.2 [21].

Another granular coarsening experiment with a ring setup consisting of 12 compartments discussed in the second part of this report. It is an extended version of a box divided

Figure 5.1: a) A freshly poured beer consists of many small foam cells, immediately starting to coarsen into larger ones. b) Close-up of a coarsening foam based on water.

Figure 5.2: Granular coarsening can be observed when a disk with granular material is shaken vertically: large heaps consume the smaller ones (from [21]).

into two compartments, with the same number of beads put in each compartment initially. A granular gas is formed by vigorously shaking the box in the vertical direction and if the shaking strength is decreased below a certain critical value, the beads cluster in one compartment [21, 15, 13]. The explanation for this behavior is that a well-filled compartment gets fuller, because of the higher number of inelastic collisions dissipating more energy compared to the dilute compartment. When the shaking strength is kept constant, this situation of one compartment filled with almost all beads and the other one left almost empty, is the steady state. There are still beads jumping from the full "cold" compartment to the dilute "hot" compartment and vice versa, but the flux in both directions is the same. In a situation with more than two compartments the same clustering effect can be observed. Only now, the final state with a single cluster is reached via transient states consisting of more than one cluster. In such a transient state the larger clusters will grow at the expense of the smaller ones, which is a coarsening process leading eventually to the stable state of one surviving cluster.

5.2 Coarsening Dynamics: Flux Model Predictions

The clustering effect for two compartments has been described in section 5.1. In order to model the coarsening phenomenon in the ring setup with 12 compartments, the flux in and out of each compartment is considered in this section.
From the two compartment experiment it can be derived that the flux function (the particle flux out of a compartment as a function of the number of particles in it) has to have a maximum for a certain number of particles. Only in this way the same flux for small and

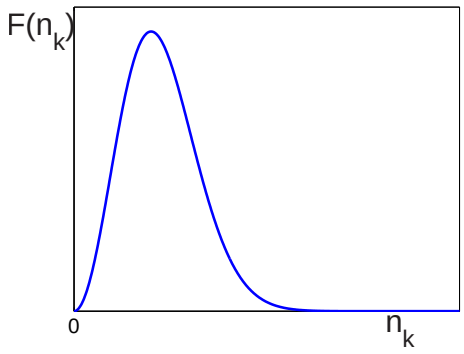

Figure 5.3: The shape of the flux function $F(n_k)$ of equation (5.1) for the inelastic case: $e < 1$.

large particle numbers can be explained. Eggers [15] proposed an average flux function for the number of particles leaving compartment k, which was rewritten for any number of N compartments by Van der Weele et al. [13]:

$$F(n_k) = An_k^2 \exp^{-N^2 B n_k^2}. \tag{5.1}$$

This flux function indeed reaches a maximum at $n_k = 1/(N\sqrt{B})$, where n_k is the fraction of particles in the k-th compartment, $\Sigma n_k = 1$. The absolute rate of the flux is determined by A. A depends on the shaking strength, on the particle properties like the radius r and the restitution coefficient e and it also depends on the surface of the slit between the compartments. This prefactor A is accounted for in the time scale. Factor B plays a more important role and will be described below. The flux function of (5.1) describes the flux to its nearest neighbors, compartments $k-1$ and $k+1$, and is shown for the inelastic case ($e < 1$) in Fig. 5.3. For a very dilute and a well-filled compartment the same flux value can be found. This is in fact very logical: A dilute compartment does not contain many particles, so the flux is low, and for a full compartment the chance to get enough kinetic energy to jump to the other side is very small as explained in section 5.1.
The dimensionless factor B of (5.1) solely determines the phase transition towards the clustered state and it takes the form [15]:

$$2D : B \propto \frac{gh}{(af)^2}(1-e^2)^2(\frac{Pr}{lN})^2, \tag{5.2}$$

$$3D : B \propto \frac{gh}{(af)^2}(1-e^2)^2(\frac{Pr^2}{\Omega N})^2. \tag{5.3}$$

Where h is the height of the wall (lower boundary of the slit), a the amplitude of the shaking, f the shaking frequency, P the total number of particles, l the width of each box (in 2D) and Ω the surface area of a compartment (in 3D). A clustered state can be reached by tuning this factor B and because everything is fixed except the amplitude a and the frequency f, it can be regarded as an inverse shaking strength. If the shaking strength is increased by means of a and f, the factor B decreases and vice versa.

The different behavior of an ordinary gas with respect to a granular gas can be inferred also from Fig. 5.3 in combination with equation (5.3). When an ordinary gas is considered, the collisions are perfectly elastic ($e = 1$) and hence $B = 0$, leading to a monotonously increasing $F(n_k)$. Thus, no clustering is possible in an ordinary gas.

Given the flux function, the time rate of change for the fraction n_k in the k-th compartment is governed by the following balance equation:

$$\frac{dn_k}{dt} = F(n_{k-1}) - 2F(n_k) + F(n_{k+1}) + \xi_k, \tag{5.4}$$

with $k = 1, 2, \ldots, N$ and periodic boundary conditions. The noise term ξ_k (with $\sum_k \xi_k = 0$) coming from the statistical fluctuations in the flux, will be neglected. So the time rate of change of n_k is equal to the flux of particles coming in from its neighbors minus the flux going out to these nearest neighbors.

From the flux, one can find the so-called bifurcation diagrams [22]. As an example, the hysteretic bifurcation diagram of $N = 5$ compartments is shown in Fig. 5.4. The uniform distribution, $n_k = 0.2$, is stable for small B (or high shaking strength). This distribution gets unstable at the bifurcation point $B_{bif} = 1$ and clusters arise. Depending on the B-value a number of "transient states" appear, which are depicted as dashed lines in Fig. 5.4. These states are actually equilibria, but unstable ones, because only the state with one cluster is stable for $B > 1$. In such a transient state the clusters fight one another until the stable one-cluster state is reached, but this may take a considerable time depending on the B-value. For a high B-value, i.e. low shaking strength, a number of transient states has to be gone through and each of them takes quite some time.
The hysteretic effect can be seen clearly in Fig. 5.4. When the one-cluster state is con-

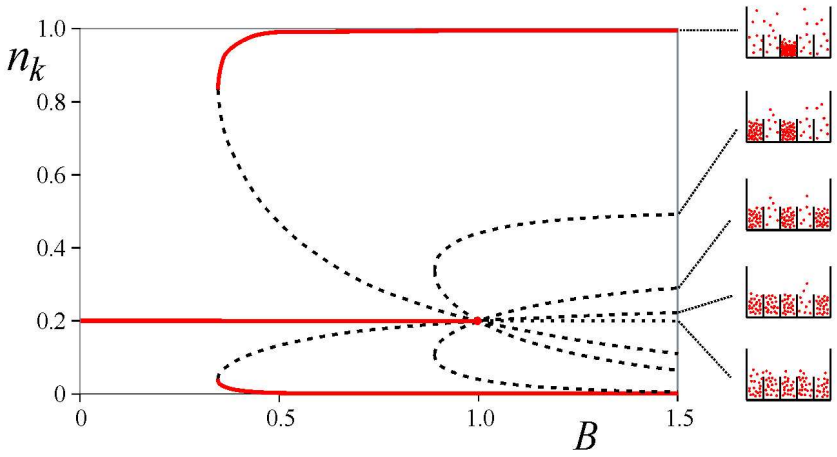

Figure 5.4: Hysteretic bifurcation diagram for $N = 5$ compartments. The stable equilibria are depicted as solid lines (red) and the unstable ones are the dashed lines (black).

sidered and the B-value is decreased, the single cluster is still in a stable equilibrium well below the bifurcation point $B_{bif} = 1$. If the increasing shaking strength approaches the critical level $B = 0.34$ the particles start to go to the nearest neighbors. For B slightly smaller than 0.34 (when the shaking strength is just above the critical value) a remarkable phenomenon called "sudden collapse" is observed: after a certain (often considerably long) time in which the cluster seems to be stable, the cluster evaporates in a few seconds spreading over all compartments. What happens is that the seemingly stable cluster is continuously leaking a small number of particles to its neighbors, thus decreasing its fraction of particles n_k, and its flux $F(n_k)$ correspondingly increases, see Fig. 5.3. This process carries on until the particle flux approaches its maximum value, speeding up the process enormously [22, 23]. At this moment the cluster collapses very abruptly.

For the ring setup with 12 compartments the same type of bifurcation diagram can be produced using the flux model, see Fig. 5.5. This figure shows that the hysteresis is even more pronounced than in the 5-compartment case of Fig. 5.4, and that the number of transient states is much larger.

The first regime of coarsening describes the growth of the clusters starting from a (nearly) uniform distribution, see Fig. 5.6a). A prediction for the particle fraction n_k of the inter-cluster compartments can be found if the continuum limit for x of equation (5.4)

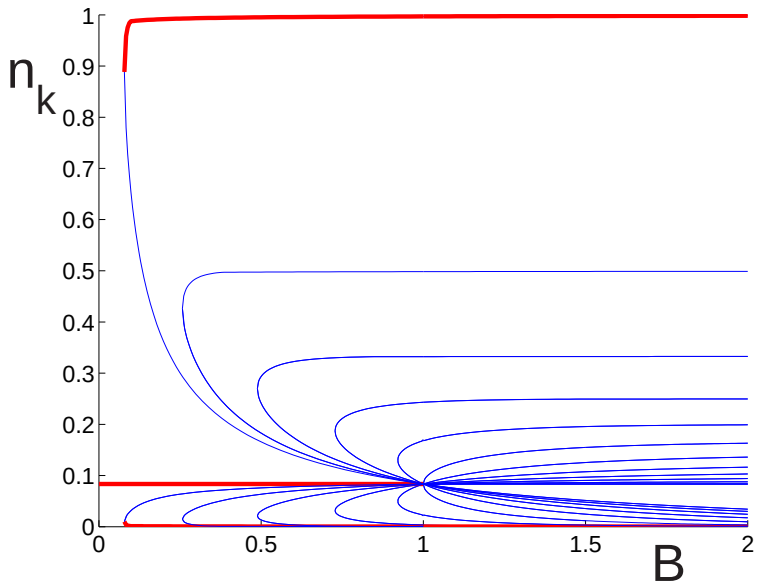

Figure 5.5: Hysteretic bifurcation diagram for the ring setup with $N = 12$ compartments. The stable equilibria are depicted as thick, red lines and the unstable ones are the thin, blue lines.

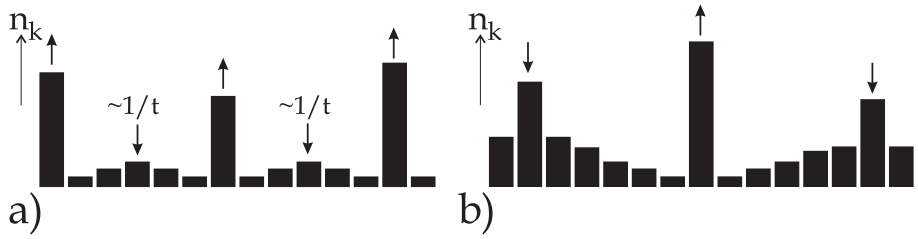

Figure 5.6: a) Sketch of the profile of the first coarsening regime, cluster growth from a uniform distribution. The prediction for n_k of the compartments between two clusters is that $n_k \propto 1/t$. b) This profile of the second coarsening regime shows the cluster-to-cluster dynamics. (The three clusters depicted here are much higher in reality.)

is taken, see also Van Bilsen [24]:

$$\frac{dn_k}{dt} \approx \triangle x^2 \frac{\partial^2 F}{\partial x^2} \approx \widetilde{A} \frac{\partial^2 n_k}{\partial x^2}. \tag{5.5}$$

In equation (5.5) is made use of the fact that $F(n_k) \approx A n_k^2$ applies for small n_k, and that $\widetilde{A} = \triangle x^2 A$. The intermediate hills are observed to maintain their basic shape during their decay, so a self-similar solution can be proposed:

$$n(x,t) = \frac{x_0^2}{\widetilde{A}t} G(\zeta), \qquad \zeta = \frac{x}{x_0}. \tag{5.6}$$

The partial differential equation (5.5) can be solved using the Ansatz of equation (5.6) (which yields an ordinary differential equation for $G(\zeta)$) and the solution is an ellipsoid. This solution (5.6) shows that the intermediate hills between the clusters decrease with time as follows:

$$n_k(t) \propto \frac{1}{t}. \tag{5.7}$$

One of the aims of the experiments discussed in section 6.3 will be to check the validity of this flux model prediction.

The clusters keep on growing larger at the expense of the intermediate dilute compartments and when the clusters have fully developed, the system enters the second regime of coarsening: the slow cluster-to-cluster dynamics. In this regime the clusters collapse one after the other, at increasing time intervals, until the final (stable) state is reached, the single cluster state.
During the slow cluster-to-cluster dynamics the profile between the clusters is no longer hill-shaped as in Fig. 5.6a), but is monotonously increasing (see Fig. 5.6b) and Fig. 5.7) from the higher cluster to the lower one. The flux $F(n_k)$ grows along the profile, in such a way that the net flux $F(n_{k+1}) - F(n_k)$ from compartment to compartment is constant.

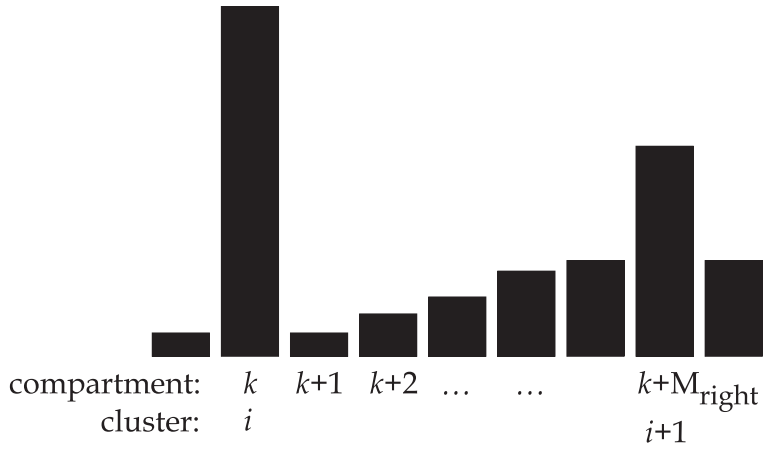

Figure 5.7: In order to describe the slow cluster-to-cluster dynamics a certain distance d apart, the indexing is switched: from k denoting the compartments, to i denoting the clusters. The heights of the clusters with respect to the intermediate compartments is in reality much higher.

Thus, the balance equation (5.4) for compartment n_k can be rewritten as follows:

$$\begin{aligned}\frac{dn_k}{dt} &= \{F(n_{k+1}) - F(n_k)\} + \{F(n_{k-1}) - F(n_k)\} \\ &= \frac{1}{d_{k,k+M_{right}}}\{F(n_{k+M_{right}}) - F(n_k)\} + \frac{1}{d_{k,k-M_{left}}}\{F(n_{k-M_{left}}) - F(n_k)\}, \quad (5.8)\end{aligned}$$

where $d_{k,k+M_{right}}$ is the distance (measured in compartments) between the clusters at k and $k+M_{right}$, and $d_{k,k-Mleft}$ is the analogous distance to the cluster on the left. Switching now from the index k (which denotes the compartments) to the index i (denoting the successive clusters), as in Fig. 5.7, this equation takes the form:

$$\frac{dn_i}{dt} = \frac{F(n_{i+1}) - F(n_i)}{d_{i,i+1}} + \frac{F(n_{i-1}) - F(n_i)}{d_{i-1,i}}. \quad (5.9)$$

The cluster-to-cluster equation (5.9) for a situation with two cluster A and B becomes

$$\frac{dn_A}{dt} = \frac{F(n_B) - F(n_A)}{d_{A,B}}, \qquad n_B \approx 1 - n_A. \quad (5.10)$$

From this the following relation for the breakdown time of the smaller cluster (which is assumed to be B in this case) can readily be extracted:

$$t_{breakdown} = d_{A,B} \int_{n_{A(0)}}^{1-\varepsilon} \frac{dn_A}{F(1-n_A) - F(n_A)} = d_{A,B}\, t_0, \quad (5.11)$$

where t_0 is the breakdown time for two clusters situated next to each other, i.e. $d_{A,B} = 1$. From equation (5.11) it can be concluded that for a one dimensional array of N compartments containing two clusters, equation (5.11) predicts the breakdown time to be

proportional to the distance $d_{A,B}$. This prediction will be checked in the experiments with the ring setup.
In the ring setup it must be taken into account that the interaction between the two clusters can act via two paths: a short path with distance d, but also a long path with distance $12 - d$ (for $d \leq 6$). The breakdown time is then found as follows, analogously to the substitution resistance of two resistors connected parallel:

$$\frac{1}{t_d} = \frac{1}{dt_0} + \frac{1}{(12-d)t_0} \quad \Leftrightarrow \quad t_{breakdown} = t_0 d(1 - \frac{d}{12}). \tag{5.12}$$

Equation (5.12) is the prediction of the flux model for two clusters situated in the ring setup with $N = 12$ compartments, the validity of which will be checked in the experiments of section 6.4.

Chapter 6

Coarsening: Experiment vs. Theory

6.1 Experimental Setup

In chapter 5 the main part of the setup, the ring setup with 12 compartments, has been mentioned briefly and a sketch of the experimental setup is shown in Fig. 6.1. The ring setup with 12 compartments is constructed with an aluminium inner cylinder and the outer wall is made out of glass. The compartments are separated by aluminium walls with $5mm$ slits at a height of $h = 29mm$. These slits prohibit the beads to jump more than one compartment in order to compare the experimental results with the simulation results. See appendix B for more properties of the ring setup and a sketch of one compartment. The ring setup is mounted on the shaker, equipped with an accelerometer. As in the Gran-

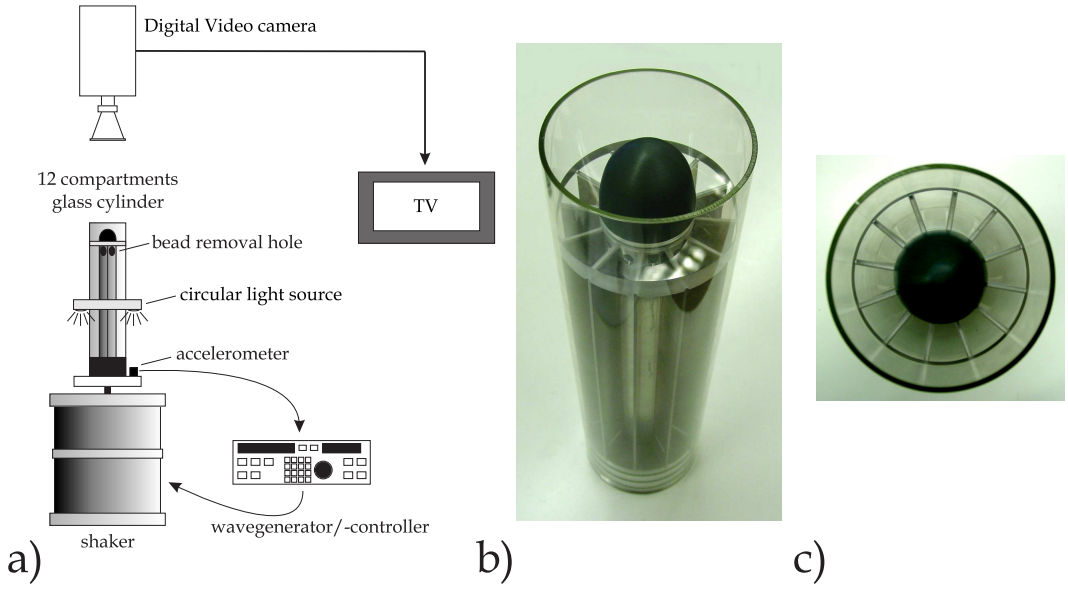

Figure 6.1: a) Sketch of the setup used for the Granular Coarsening experiments with the b) ring setup consisting of $N = 12$ compartments. c) Top view of the ring setup.

ular Leidenfrost effect experiments this accelerometer maintains the right shaking strength in combination with the wavegenerator/-controller, see section 2.2 on page 7.
A circular fluorescent lamp was placed around the cylinder and used for the illumination of the lower part of the compartments. This light source had only one disadvantage: three compartments are less illuminated due to the gap at the start and end of the circular light bulb. This problem could not be solved experimentally, but during the data analysis this effect is taken into account.
To record the experiments a Digital Video (DV) camera was used and it was situated straight above the setup on a large tripod. The camera was focussed by hand at a height a little bit above the beads in a cluster. When the beads are in focus, white spots of the lamp are recorded and they are hard to analyze correctly. Those spots are not recorded when the beads are a little out of focus. The DV-camera was linked to a television to align the camera position exactly above the ring setup in such a way that all 12 compartments are of the same size. During the experiments the progress could be checked on the television too in order to determine when an experiment was ready to be stopped.
A total number of $P = 480$ red glass beads of diameter $d = 2.5mm$ are used: if more beads are used in the setup, the stable one-cluster state will be so full of beads that the compartment cannot hold them without spilling beads into the neighboring compartments. So for a clear clustered state this number of beads was determined to be optimal. If considerably less beads are put in the setup, statistical fluctuations become too important for the adopted mean field description. In that case, the noise term ξ_k in equation (5.4) should not be neglected.
Static electricity is a general problem in granular experiments, see section 2.3. In the granular coarsening experiments static electricity can build up due to the long shaking times of typically 10 minutes per experiment. If many experiments are performed in a row, the beads can be observed to stick to the glass wall. Whenever the unwanted effect of static electricity is observed, the glass beads are taken out and the lid of the ring setup is removed in order to let the setup "breathe" and to neutralize the charge imbalance.
In all experiments the shaking amplitude was fixed at $a = 1.0mm$, so the shaking strength was only changed by tuning the frequency f. The bifurcation point $B_{bif} = 1$, where the uniform distribution is starting to get unstable, was determined to be located around a frequency of $f = 43Hz$. From the experiment it was also determined that for a frequency $f < 25Hz$, the beads are not able to jump to other compartments anymore.

6.2 Data Processing

The experiments recorded on a DV-tape can be converted without any loss of quality to single pictures of which every 25th pictures was saved to be analyzed, corresponding to one frame per second. Such a picture sequence is analyzed using a filter for the RGB-values (Red Green Blue) in order to obtain all the red bead pixels. This filter works with two thresholds, one minimal threshold for the color red and one threshold for the colors green

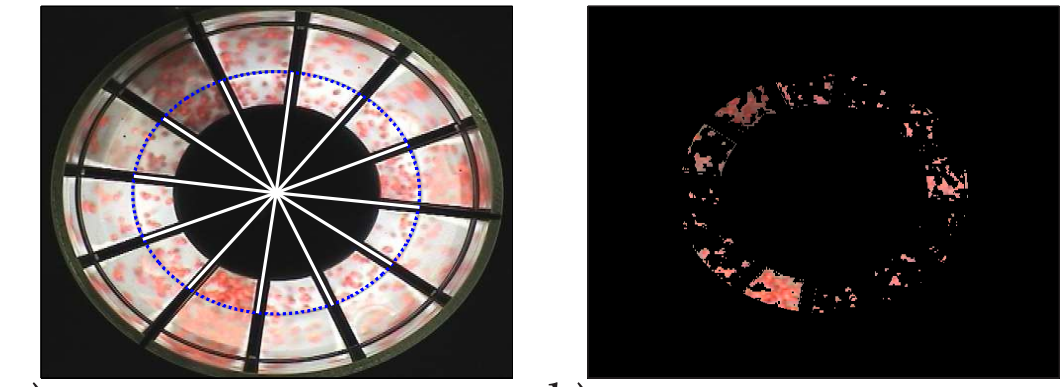

Figure 6.2: a) An original experimental picture together with the applied masks to detect the bottom (blue circle) and the 12 compartments (white lines). b) The corresponding processed picture from which the red pixels are assigned to the 12 compartments. It has been processed using the masks defined in a) and using a threshold for the RGB-value to track most of the red bead pixels, without tracking too much of the background.

and blue, which need to be below this second threshold. By tuning these two thresholds, most of the red bead pixels are picked out of the original experimental pictures without picking also some background pixels. Such a pixel has a Red-value larger than the red-threshold and a Green-Blue-value smaller than the corresponding threshold. For the three less illuminated compartments different threshold values are applied in order to get the same result as for the 9 uniformly illuminated compartments.
Besides filtering out the red pixels, the reflections of the beads in the glass cylinder wall cut from the original pictures by using a mask based on the bottom. In this way the number of pixels in a cluster is underestimated, because of the parallax the top beads near the cylinder wall will not be counted. This restriction will not affect the final results, because this method of counting red pixels does not provide any precise quantitative information anyhow about the number of beads in a cluster.
The separation walls between the compartments are manually selected for each experiment, whereafter the red pixels of every recorded frame can be counted and assigned to one of the 12 compartments, see the typical experimental picture and its processed version in Fig. 6.2. In this way the number of red pixels in a particular compartment follows the clustering processes going on in the setup.

6.3 Starting from a Uniform Distribution

The first experiments were carried out starting from a uniform distribution shaken at different frequencies, i.e. different B-values. A uniform distribution was first formed by carefully putting 40 glass beads in each compartment, but it can also be accomplished by vigorous shaking at $f = 80Hz$ for a few minutes. (The B-value corresponding to $f = 80Hz$

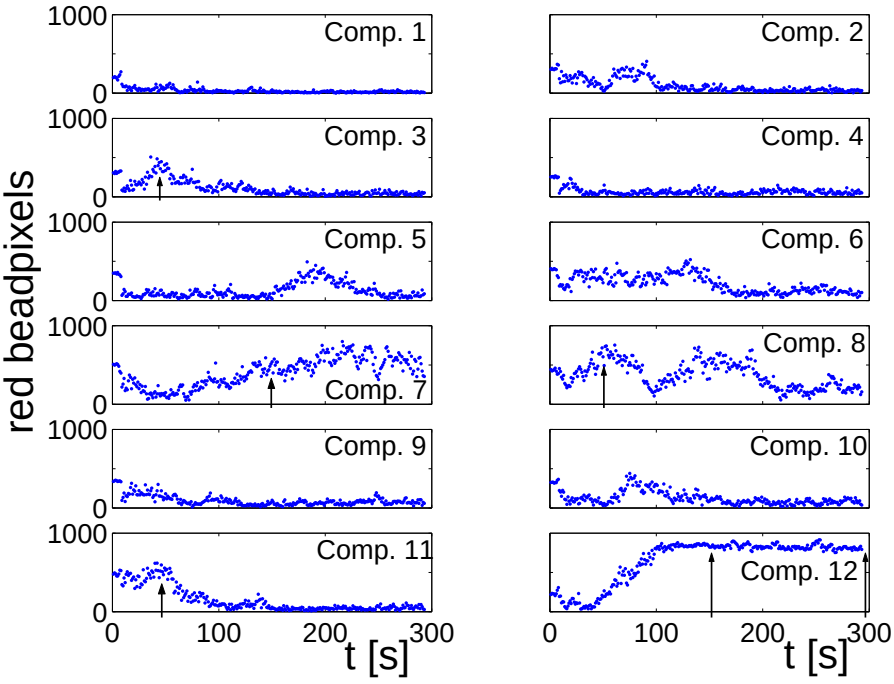

Figure 6.3: For each of the 12 compartment the number of red bead pixels is recorded every second for an experiment starting from a uniform distribution shaken at $f = 37Hz$. The arrows located at $t = 50$, $t = 150$ and $t = 300$ indicate the clusters present, in this way showing the transient states for $t = 50$ and $t = 150$. Compartment number 9,10 and 11 were less illuminated.

is lower than the value for which the single cluster state is still stable). Experimentally it has been checked that both methods of forming a uniform distribution give the same results, so the vigorous shaking method was adopted to save time.
Immediately after processing the first test experiments, the conclusion had to be drawn that from the resulting bead pixel plots nothing quantitative could be said about the processes going on in the regions between the clusters. See Fig. 6.3 for a typical example of such a pixel plot. Note in particular the difference in the number of counted red pixels for the different compartments, in the initial *uniform* distribution. Therefore, these pixel plots can not be used to check the validity of the inter-cluster relation of equation (5.7).

t [s]	cluster in compartment(s)
50	3,8,11
150	7,12
300	12

From the typical pixel plot of Fig. 6.3, the successive transient states for this $f = 37Hz$ experiment can be determined and are shown in the table. Here experimental evidence is found for the slow cluster-to-cluster dynamics of the second coarsening regime. In this

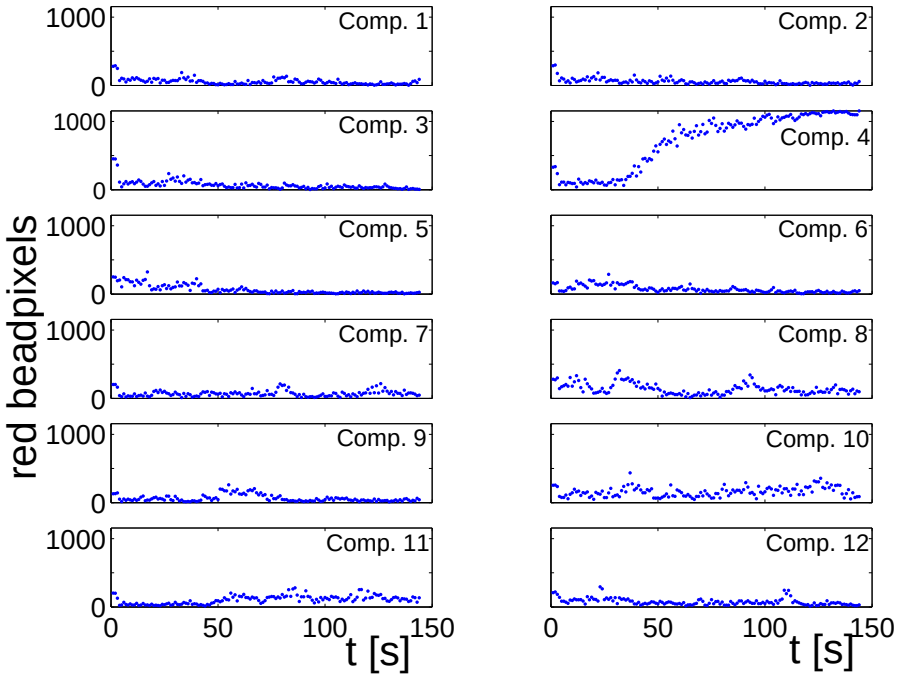

Figure 6.4: Pixel plot for an experiment at $f = 41$, i.e. a lower B-value than in Fig. 6.3. No transient states are observed and the system goes from a uniform distribution immediately to the stable one-cluster state. Compartment number 9,10 and 11 were less illuminated.

experiment the clusters collapse one after the other at increasing time intervals: $\Delta t \approx 100s$ from 3 to 2 clusters and $\Delta t \approx 150s$ for the system to go to the final stable state of a single cluster. So for this B-value it is observed that two transient state had to be gone through. In experiments with higher B-values, i.e. lower shaking strength, more transient states are observed, and for a longer time. On the other hand, for B-values near B_{bif} no transient state is observed anymore: from the uniform distribution the system directly goes to the stable single cluster state, see Fig. 6.4.

From the experiments performed with shaking frequency ranging from $f = 35 - 43Hz$ the pixel plots, like the ones shown in Fig. 6.3 and Fig. 6.4, are analyzed in order to get the cluster time $t_{cluster}$, for which the winning cluster is established. Fig. 6.5 demonstrates how the cluster time is determined for a winning cluster: it is the intersection between the constant horizontal line for an established cluster and the rising straight line when the cluster is gathering glass beads.

Fig. 6.6 shows that the cluster time $t_{cluster}$ decreases approximately linearly with the shaking frequency f. Thus, for lower shaking strength it takes longer for the winning cluster to establish as expected, because a smaller f corresponds to a higher B-value and the prefactor A of equation (5.1) decreases for a higher B-value. Fewer beads are jumping from compartment to compartment and therefore it takes longer for the winning cluster to establish.

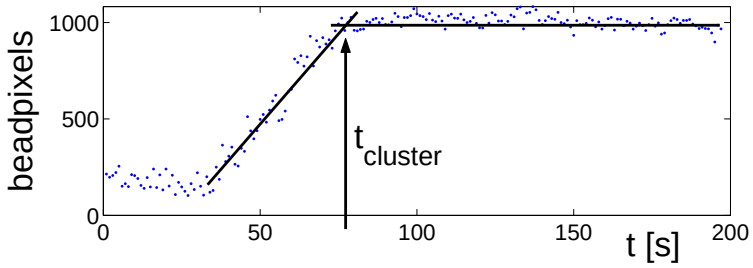

Figure 6.5: The cluster time $t_{cluster}$ is determined by the intersection of the rising straight line and the horizontal line of the winning cluster.

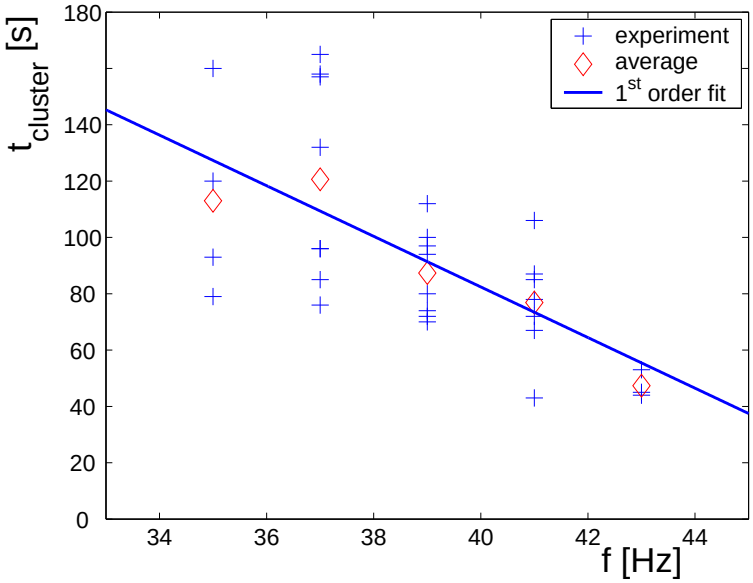

Figure 6.6: The cluster time $t_{cluster}$ is determined for experiments at various frequencies f (blue plus signs). For every set of experiments at a fixed frequency, the average cluster time was determined (red diamonds). The linear fit indicates that the cluster time decreases roughly linearly with the shaking frequency.

From this cluster time plot it can also be observed that for lower shaking frequencies the results found for the cluster time are considerably more fluctuating than for higher frequencies. A plausible explanation is that for lower shaking strengths just a few beads are jumping from compartment to compartment. Therefore, the system is more sensitive to the initial distribution than for higher shaking strength. In experiments for low shaking frequencies it has been observed that when the initial distribution is not perfectly uniform, the surviving cluster emerges quickly. So, in general it is important for these experiments to provide an initial distribution, which is as close to uniform as possible. For experiments at a relatively low shaking strength, it is even of more importance to provide a perfectly uniform distribution in order to get reliable results.

6.4 Competition between Two Clusters

The second kind of experiments started with two competing clusters a certain distance d apart, where d is defined as the shorter path in the ring setup. As mentioned in section 5.2, the two-cluster state is an unstable equilibrium, so only one will survive and the time it takes before one of them breaks down $t_{breakdown}$ is described by equation (5.12).
In order to check relation (5.12), two clusters are put in the ring setup with the intermediate 10 compartments completely empty. Both clusters were not of the same size, but one was filled with $P = 280$ red beads and the other one with the remaining $P = 200$ glass beads. Thus, the winning cluster is known (the statistical fluctuations are well below this difference) and the process of one cluster surviving the other is much faster. The absolute winning time will be changed of course, but it only influences t_0 (see equation (5.12) in section 5.2) and therefore the prediction for the breakdown times remains the same.
All experiments have been performed using the same frequency of $f = 41Hz$ and fixed amplitude $a = 1.0mm$. The pixel plot of Fig. 6.7 is a good example of how the cluster containing 200 beads suddenly breaks down. The breakdown time is determined roughly the same as the cluster time as indicated in Fig. 6.7. It is determined from the intersection of the falling line and the horizontal straight line of an almost empty compartment, in the

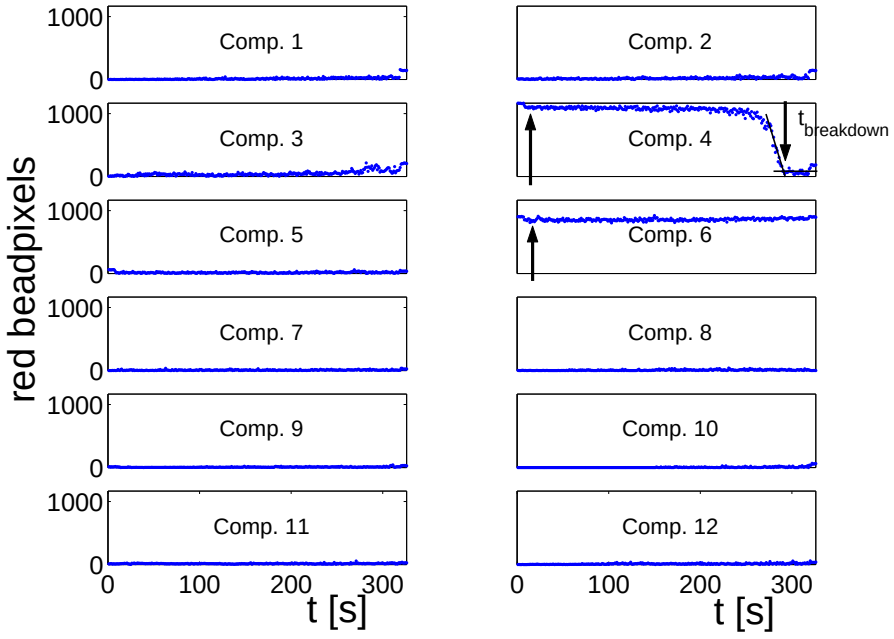

Figure 6.7: Pixel plot of an experiment with initially two clusters (in compartment 4 and 6) a distance $d = 2$ apart. The breakdown time of the $P = 200$ cluster in compartment 4 is determined to be $t_{breakdown} = 292s$.

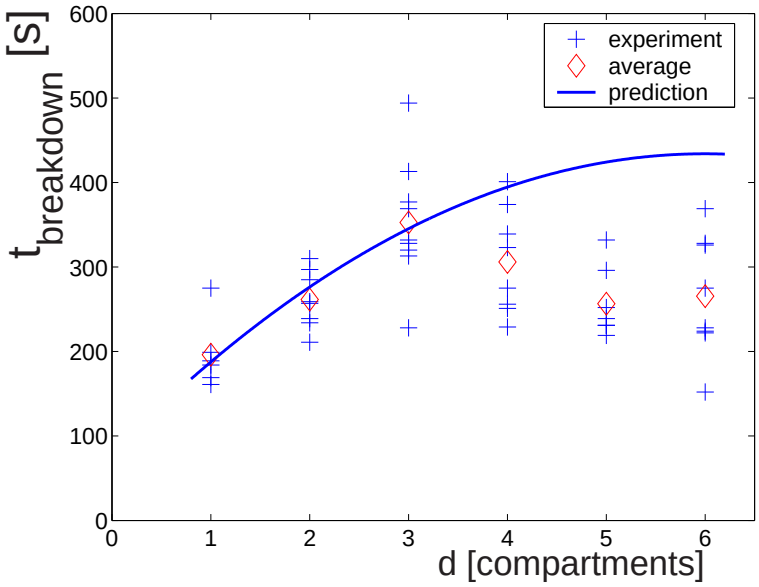

Figure 6.8: Starting with two clusters ($P = 200$ and $P = 280$ glass beads) a number of compartments d apart, the smaller cluster will break down in $t_{breakdown}$. The breakdown time as a function of the distance d (blue plus signs) is averaged for every d-value (red diamonds). The solid, blue line shows the prediction of equation (5.12) fitted for $d = 1, 2, 3$ (corresponding to $t_0 = 79s$).

same spirit as in Fig. 6.5. The breakdown times determined for the experiments starting with two clusters at various distances apart are plotted in Fig. 6.8. Fig. 6.8 shows the experimental results for the breakdown time for two clusters in the ring setup at various distances apart. The prediction of (5.12) seems to be valid for small d; accordingly, the prediction depicted in Fig. 6.8 as a solid blue line is based on the experimental breakdown times for $d = 1, 2, 3$ (corresponding to $t_0 = 79s$). This prediction clearly does not hold for the results for $d > 3$.

A word of caution is necessary: The two-cluster results shown here have to be treated very carefully, because three additional experiments for various d were carried out two months after the ones depicted in Fig. 6.8 and the corresponding breakdown times were a factor 2 to 3 higher. The reason for this difference is not clear yet. The different, drier weather conditions may have affected the results via more static electricity, causing the beads to stick to the wall. Besides, these last experiments were performed with new red glass beads and this can also affect the breakdown time. Because of the apparent sensitivity to the precise experimental conditions, more experiments with red glass beads are needed to investigate the validity of the breakdown time equation (5.12). The experiments may have to be performed with metal beads as well, because these beads will build up less static electricity than glass beads.

6.5 Coarsening or Sudden Collapse?

According to the proposed relation (5.12), the breakdown time would monotonously increase with the distance d between the clusters. Experimental proof of a monotonously increasing relation for the breakdown time has clearly been provided for $d \leq 3$ in Fig. 6.8. For $d > 3$, however, the breakdown time is stabilizing around a certain value, which is an indication of a lack of interaction between the clusters. The same saturation effect has been found before in Molecular Dynamics simulations (in a linear array of compartments) by Van Bilsen [24]. Here we propose an explanation for this saturation in terms of the sudden collapse effect mentioned earlier in section 5.2.
The saturation value may in fact be the collapse time for a single $P = 200$ cluster, i.e. for the smaller cluster independent of the larger one. In this picture, the sudden collapse for $d \geq 4$ occurs before the "transport band" between the clusters has been built up, see Fig. 5.7. This is possible due to the fact that these experiments started with two isolated clusters, with no beads in the intermediate compartments, which is different from a transient two-cluster state emerging from a uniform initial distribution.
In the performed experiments the development of the transport bands may well take more time than the collapse time of the smaller cluster. Effectively, the ring setup then contains two independent systems with $P_1 = 200$ and $P_2 = 280$ beads, respectively. For the smaller cluster this implies that the effective B-value is much smaller than the B-value for the total system, because $B \propto P^2$, see equation (5.3). With $P_{cluster}/P_{total} = 200/480$, the effective B-value is only 0.17 of the B-value of the total system. This effective value can easily be situated below the critical B-value required for the sudden collapse ($B = 0.08$ for $N = 12$ compartments), as shown in Fig. 6.9.

From a series of 7 experiments starting with only a single $P = 200$ bead cluster, the average collapse time was determined to be $t_{collapse} = 438s$. This is roughly 100 seconds above the saturation value of Fig. 6.8. The discrepancy can be attributed to the different conditions in the collapse experiments as compared to the experiments of Fig. 6.8. As mentioned already at the end of the previous section 6.4, it would be worthwhile to redo the experiments under more carefully controlled conditions, preferably with metal beads. This will clarify whether the saturation is indeed a sudden collapse phenomenon.
Apart from experiments, it is advisable to check the proposed explanation for the saturation also by means of Molecular Dynamics simulations.

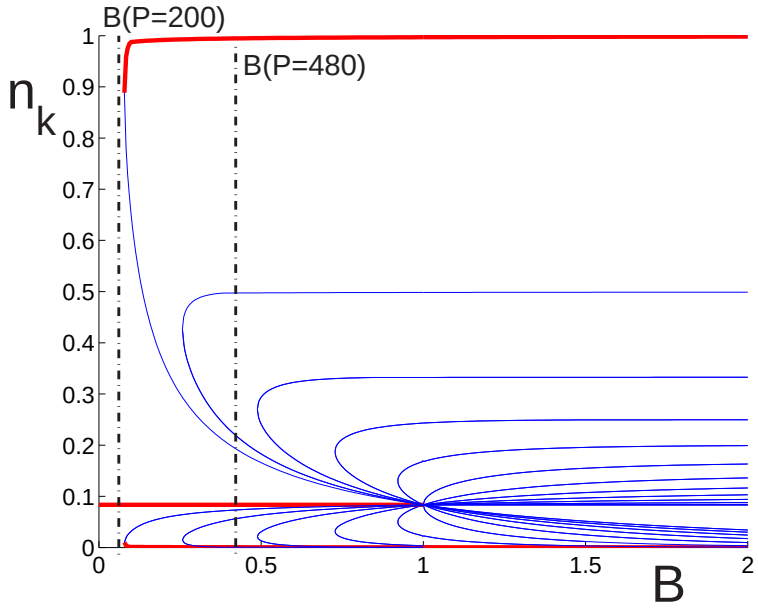

Figure 6.9: Bifurcation diagram for $N = 12$ compartments with dash-dotted lines drawn for the B-values corresponding to $P = 480$ and $P = 200$ glass beads. The saturation shown in Fig. 6.8 may be explained by the sudden collapse of the smaller (independent) $P = 200$ cluster, indicated here by the $B(P = 200)$-value, which lies below the critical B-value of $B = 0.08$ for $N = 12$ compartments.

Appendix A

Equipment

- Shaker: Brel & Kjær (Denmark), Type: Exciter Body Type4802
- Gen Purpose Head Type 4817: current limit=43 amperes rms, displacement limit=0.75 inches=19 mm, head constant=1.20 inches/volt sec, bolt torque limit: 50 inch lbs=0.57 kgm
- Power Amplifier: Brel & Kjær (Denmark), Type: 2708
- Wavegenerator/-controller: Brel & Kjær (Denmark), Type: Vibration Exciter Control Type 1050
- High-speed camera: Kodak Ektapro Model 2000, max. framerate=2000 fps

Appendix B

Ring Setup

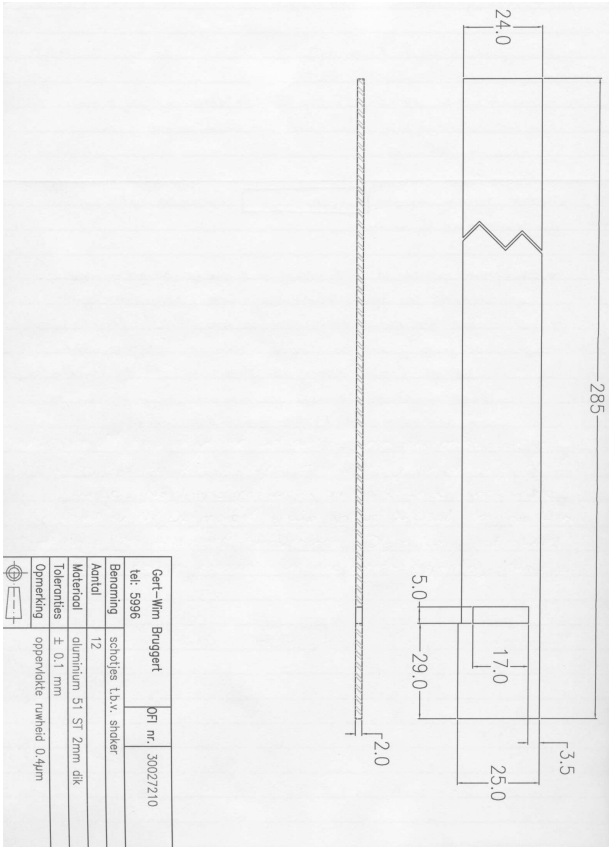

Figure B.1: A sketch with dimensions of a compartment of the $N = 12$ compartment ring setup: Surface area of 1 compartment: $\Omega = 241mm^2$, Surface of slit: $85mm^2$, Outer cylinder diameter: $104mm$ and Inner cylinder diameter: $80mm$.

Bibliography

[1] H. M. Jaeger, S. R. Nagel, and R. P. Behringer. Granular solids, liquids, and gases. *Rev. Mod. Phys.*, 68:1259–1273, 1996.

[2] H. M. Jaeger, S. R. Nagel, and R. P. Behringer. The physics of granular materials. *Physics Today*, 49:32–38, 1996.

[3] I. Goldhirsch. Rapid granular flows. *Annu. Rev. Fluid Mech.*, 35:267–293, 2003.

[4] L.P. Kadanoff. Built upon sand: theoretical ideas inspired by granular flows. *Rev. Mod. Phys.*, 71:435–444, 1999.

[5] T.M. Knowlton, J.W. Carson, G.E. Klinzing, and W-C. Yang. The importance of storage, transfer and collection. *Chem. Eng. Prog.*, 90:44–54, 1994.

[6] B. Behringer. Collapsing bin. *www.phy.duke.edu/∼bob/.*

[7] J.G. Leidenfrost. On the fixation of water in diverse fire. *Int. J. of Heat and Mass Transfer*, 9:1153–1166, 1966.

[8] C. Pounder. Leidenfrost's phenomenon. *www.geocities.com/CapeCanaveral/Lab/-8063/leidenfr.htm.*

[9] J. Walker. Boiling and the leidenfrost effect. *www.wiley.com/college/phy/-halliday320005/pdf/leidenfrost_essay.pdf.*

[10] P.G. Eshuis, M.C.F. Vervoorn, and M. Versluis. Droplet of water on a hot surface, or how to walk over hot coals. *Report for the course "Experimental Methods in Fluid Mechanics", Physics of Fluids Group, University of Twente*, 2002.

[11] Y. Lan and A. D. Rosato. Macroscopic behaviour of vibrating beds of smooth inelastic spheres. *Phys. Fluids*, 7:1818–1831, 1995.

[12] B. Meerson, T. Pöschel, and Y. Bromberg. Close-packed floating clusters: granular hydrodynamics beyond the freezing point? *Phys. Rev. Lett.*, 91:024301, 2003.

[13] K. van der Weele, D. van der Meer, M. Versluis, and D. Lohse. Hysteretic clustering in granular gas. *Europhys. Lett.*, 53:328–334, 2001.

[14] C.K. Adams. *Nature's electricity.* Blue Ridge Summit, PA: Tab Books, 1st edition, 1987.

[15] J. Eggers. Sand as maxwell's demon. *Phys. Rev. Lett.*, 83:5322–5325, 1999.

[16] E. L. Grossman, T. Zhou, and E. Ben-Naim. Towards granular hydrodynamics in two dimensions. *Phys. Rev. E*, 55:4200–4206, 1997.

[17] J.T. Jenkins and M.W. Richman. Boundary conditions for plane flows of smooth nearly elastic circular discs. *J. Fluid Mech.*, 171:53–69, 1986.

[18] W.T. Vetterling W.H. Press, S.A. Teukolsky and B.P. Flannery. *Numerical Recipes.* Cambridge University Press, 2nd edition, 1992.

[19] R.P.H.M. Bergmann. Measurements and simulations of bubble systems in an acoustic field. *Master Thesis, Physics of Fluids Group, University of Twente*, 2003.

[20] S.A. Koehler S. Hilgenfeldt and H.A. Stone. Dynamics of coarsening foams: Accelerated and self-limiting drainage. *Phys. Rev. Lett.*, 86:4704–4707, 2001.

[21] H.J. Schlichting and V. Nordmeier. Strukturen im sand. *Math. Naturwiss. Unterr.*, 49:323–332, 1996.

[22] D. van der Meer, K. van der Weele, and D. Lohse. Bifurcation diagram of compartmentalized granular gases. *Phys. Rev. E*, 63:061304, 2001.

[23] D. van der Meer, K. van der Weele, and D. Lohse. Sudden collapse of a granular cluster. *Phys. Rev. Lett.*, 88:174302, 2002.

[24] A. van Bilsen. Fluxes and coarsening of a compartmentalized granular gas, a molecular dynamics approach. *Master Thesis, Physics of Fluids Group, University of Twente*, 2002.